

KINEMATICS OF THE CENTRAL STARS POWERING BOWSHOCK NEBULAE AND THE LARGE MULTIPLICITY FRACTION OF RUNAWAY OB STARS

HENRY A. KOBULNICKY¹ AND WILLIAM T. CHICK¹

¹*Department of Physics & Astronomy
 University of Wyoming
 1000 E. University
 Laramie, WY 82070, USA*

ABSTRACT

OB stars powering stellar bowshock nebulae (SBNe) have been presumed to have large peculiar velocities. We measured peculiar velocities of SBN central stars to assess their kinematics relative to the general O star population using *Gaia* EDR3 data for 267 SBN central stars and a sample of 455 Galactic O stars to derive projected velocities v_{2D} . For a subset of each sample we obtained new optical spectroscopy to measure radial velocities and identify multiple-star systems. We find a *minimum* multiplicity fraction of $36 \pm 6\%$ among SBN central stars, consistent with $>28\%$ among runaway Galactic O stars. The large multiplicity fraction among runaways implicates very efficient dynamical ejection rather than binary-supernova origins. The median v_{2D} of SBN central stars is $v_{2D}=14.6 \text{ km s}^{-1}$, larger than the median $v_{2D}=11.4 \text{ km s}^{-1}$ for non-bowshock O stars. Central stars of SBNe have a runaway ($v_{2D}>25 \text{ km s}^{-1}$) fraction of $24^{+9}_{-7}\%$, consistent with the $22^{+3}_{-3}\%$ for control-sample O stars. Most (76%) of SBNe central stars are not runaways. Our analysis of alignment (Δ_{PA}) between the nebular morphological and v_{2D} kinematic position angles reveals two populations: a highly aligned ($\sigma_{PA}=25^\circ$) population that includes stars with the largest v_{2D} (31% of the sample) and a random (non-aligned) population (69%). SBNe that lie within or near H II regions comprise a larger fraction of this latter component than SBNe in isolated environments, implicating localized ISM flows as a factor shaping their orientations and morphologies. We outline a new conceptual approach to computing the Solar LSR motion, yielding $[U_\odot, V_\odot, W_\odot] = [5.5, 7.5, 4.5] \text{ km s}^{-1}$.

1. INTRODUCTION

1.1. Bowshock Nebulae and their Central Stars

Stellar bow shock nebulae (SBNe) constitute a distinctive class of arcuate interstellar nebulae flanking a central star traveling supersonically through the interstellar medium, first identified in association with ζ Oph and LL Ori (Gull & Sofia 1979). These nebulae contain swept-up stellar wind material and trapped ISM at a circumstellar distance where the momentum flux of the ISM balances that of the stellar wind (Wilkin 1996, 2000). The compressed and heated material of the nebula is most easily seen in the infrared continuum, though some SBNe have detectable emission lines including H α or O III (Gull & Sofia 1979; Brown & Bomans 2005). As more SBNe have been discovered with advances in angular resolution and sky coverage of infrared surveys, these nebulae have generated increasing interest as laboratories to explore the properties of both the central star and the ISM interactions forming the nebular structure. SBNe and SBN-like objects surround a wide variety of stars including red supergiants (Noriega-Crespo et al. 1997; Gvaramadze et al. 2014), pulsars (Wang et al. 2013), externally ionized proplyds (Bally et al. 1998), and even an A dwarf (δ Vel, Gáspár et al. 2008). Chick et al. (2020, hereafter Paper I) conducted a spectroscopic survey of 84 cataloged SBN-candidates (Kobulnicky et al. 2016, hereafter K16) and determined that $>95\%$ were O and early B stars, in agreement with theoretical expectations (Weaver et al. 1977; Mac Low et al. 1991; Comeron & Kaper 1998).

Hydrodynamical simulations indicate that the density of the ambient ISM and the velocity differential between the ISM and the central star are both significant factors in the creation of an observable SBN (Comeron & Kaper 1998;

Meyer et al. 2014, 2016). Observable SBNs likely require ambient interstellar densities of $\gtrsim 1\text{--}5 \text{ cm}^{-3}$ (Kobulnicky et al. 2018; Henney & Arthur 2019), making it less likely that SBNs can form or be detected inside H II regions that efficiently heat and expel the ISM material (Hills 1980; Goodwin & Bastian 2006; Dale et al. 2012) or in other rarefied environments. The star-ISM velocity differential may be provided by the motion of the star (van Buren & McCray 1988; van Buren et al. 1990; Mac Low et al. 1991; van Buren & Mac Low 1992) or by a bulk ISM flow impinging upon a stationary star (i.e., “in-situ” bowshocks; Povich et al. 2008), and perhaps a combination of both. Alternatively, the stellar wind momentum flux may be supplemented (or even dominated) by stellar radiation pressure (van Buren & McCray 1988), particularly around late-O stars in the “weak wind regime” (Ochsendorf et al. 2014a,b; Henney & Arthur 2019). The diverse range of interaction types has given range to an equally diverse nomenclature of SBN subtypes, one still in the process of being standardized. Some authors (Henney & Arthur 2019) have suggested three major subtypes: traditional “bow shocks” where a thick shell of gas and dust forms about a dust-free shocked wind-supported (or radiation-supported) inner layer, “bow waves” where a thin shell of unshocked gas and dust forms due to the star’s radiation pressure acting on the dust and a gradual deceleration by gas-dust drag, and “dust waves” where the gas and dust decouple and a thin dusty shell forms supported by radiation pressure but ISM gas continues to flow. Variations and hybrids of each of these models have been proposed as well (van Marle et al. 2011). Throughout this work, we will refer to all of these arc-shaped nebulae as SBNs, acknowledging that this sample may contain some or all of these physically distinct subtypes. Henney & Arthur (2019) analyzed the 20 SBNs from Kobulnicky et al. (2018) and found 15 to be bow shocks, two likely bow waves, and three ambiguous objects.

The presumption that SBNs require supersonic (but not hypersonic) star-ISM velocity differentials and the need to form in denser regions of the ISM than their natal clusters suggests that “runaway” stars (Blaauw 1961) are good candidates to produce SBNs. Runaways exhibit large peculiar velocities, having been ejected from their natal clusters via N-body dynamical interactions (Poveda et al. 1967; Spitzer & Mathieu 1980) or by supernovae in binary systems (Zwicky 1957; Blaauw 1961). Indeed, K16 found 70% of their SBN central stars were in “isolated” environments away from H II regions. A minority of sources (7%) were co-located on the sky with H II regions. Although the threshold for runaway velocities varies by author, most studies agree on velocities between 28 km s^{-1} (Tetzlaff et al. 2011) and 40 km s^{-1} (Blaauw 1961), with most modern works adopting a three-dimensional peculiar velocity threshold of 30 km s^{-1} (Gies & Bolton 1986). Additionally, most runaways are OBA-type stars (Tetzlaff et al. 2011; de la Fuente Marcos & de la Fuente Marcos 2018), though this may be a selection effect due to their large luminosities. While runaways provide a seemingly natural solution to both the ISM density and velocity differential requirements to form an SBN, it is clear that not all central stars supporting SBNs are runaways and not all runaways support observable SBNs. Some studies have found SBNs that are aligned with ISM flows emanating from H II regions, suggesting the presence of an in-situ SBN (Gull & Sofia 1979; Povich et al. 2008). Similarly, Bodensteiner et al. (2018) found candidate SBNs that show significant misalignment between their nebular morphological axis and their stellar proper motion vectors. Peri et al. (2012, 2015) searched archival infrared images of known OB runaway stars and found that only 15% produced SBNs observable in the infrared continuum. Based on these works, it appears that detectable SBNs require a specialized set of circumstances. Being a runaway OB star alone is not sufficient.

1.2. Runaway Stars and their Origins

Observations indicate that runaway and “walkaway” stars (peculiar velocities $<30 \text{ km s}^{-1}$) comprise the majority of field OB stars—those lying outside known H II regions and young clusters. de Wit et al. (2005) found that only 4% of field stars could not be associated known associations and star forming regions, implying that very few form in isolation. While some additional OB stars may have formed in isolated environments (Oey et al. 2018), field and cluster OB stars are statistically indistinguishable, except that runaway O stars have later spectral types than those in clusters (van den Bergh 2004). It is likely that isolated formation of O stars, if possible, is extremely uncommon.

Kinematic investigations O stars have yielded significantly different runaway fractions depending on the particular observational selection criteria (e.g., definition of runaway velocity threshold) or theoretical modeling approach. Even studies that draw samples of stars from the same catalogs can generate disparate results. For example, based upon the radial velocities of stars from the catalogs of Rubin et al. (1962) and Cruz-González et al. (1974), Stone (1979) used a 40 km s^{-1} velocity threshold to find an OB runaway fraction of $49\pm 10\%$, whereas Gies & Bolton (1986) used a 30 km s^{-1} velocity threshold to find a runaway fraction of 10–25% for O stars and 2% for early B stars. The majority of studies identify runaways based upon peculiar radial velocities or peculiar transverse velocities alone. Few studies incorporate all three velocity components. Assuming the distribution of stellar velocities is isotropic, studies based

upon the two components of proper motion instead alone will underestimate the true runaway fraction by 22% (i.e., $\sqrt{3}/2$; Lamb et al. 2016). By a similar reasoning, studies based upon radial velocity alone may underestimate the true fraction by as much as 73% (i.e., $\sqrt{3}/1$).

In the seminal work on runaway O stars, Blaauw (1961) adopted a 3D runaway threshold of 40 km s^{-1} to find a runaway fraction of 1.5% for early-B stars, 2.5% for B0 stars, and 21% for late-O stars. Stone (1979) reanalyzed archival Yerkes Observatory plates to measure the 2D peculiar velocities of 47 O4–B2 stars. Using a runaway threshold of 40 km s^{-1} they found an OB runaway fraction of $49 \pm 10\%$, though Gies & Bolton (1986) note that this sample may have been biased toward runaways due to the magnitude cut preferentially selecting stars with low extinction. Gies & Bolton (1986) observed a population of 36 OB stars selected based on previous identification as high-radial-velocity sources complete to $V=8$ mag and as faint as $V=11$ mag. After applying a statistical correction to their observations to account for the sampling bias, they determined a runaway fraction of 2% for early-B and 10% for O stars. Stone (1991) fit a bimodal distribution to the observed velocities of O stars to find raw runaway fractions of 17.4%, 13.4%, 9.5% for 30, 35, and 40 km s^{-1} thresholds, respectively. After applying a statistical correction for incompleteness the corrected O star runaway fraction was 46% (Stone 1991). de Wit et al. (2005) examined the O stars identified as field objects by Mason et al. (1998) and found 22 of the 43 (51%) to be runaways based upon their 3D peculiar motions. It should be noted that field populations would be expected to have higher velocities due to their separation from stellar associations and clusters. Lamb et al. (2016) identified a sample of 374 “field” OB stars in the Small Magellanic Cloud. Deriving peculiar radial velocities based upon the radial velocities of nearby gas clouds, they found a lower limit field OB star runaway fraction of $11.3 \pm 2.2\%$, though as noted above, they estimate the true runaway rate may be as much as twice their reported rate if proper motions were included. Based upon a statistical analysis of Gaia DR1 (Gaia Collaboration et al. 2016a) proper motions of Galactic O-Star Catalog stars (version 4.1), Maíz Apellániz et al. (2018) found a runaway fraction of $6.7 \pm 1.1\%$. Seemingly, the only consistent result between these studies is a disjunction between the runaway fractions of O and B stars, with O stars being much higher. These disparate results beg for reexamination with the improved proper motions of *Gaia* EDR3 data and radial velocities.

Despite the large dispersion in observed runaway fraction, these observational studies conflict with simulations, which predict very low fractions. Two mechanisms for generating runaway stars have been proposed: the binary supernova scenario (BSS), where stars with close binary companions are ejected when the more massive component undergoes an asymmetric core-collapse supernova, and the dynamical ejection scenario (DES), where stars are ejected through N-body interactions. Hybrids models have also been proposed to explain the isolated systems of de Wit et al. (2005) through the dynamical ejection of a binary system which then undergoes the BSS. Another hybrid idea involves a supernova in a triple system that ejects a high-velocity close binary (Gao et al. 2019). Studies of the DES mechanism generally find higher proportions of stars achieving runaway velocities and higher fractions of multiplicity among those runaways than the BSS mechanism.

Investigations of the efficacy of the BSS generally rely upon population synthesis models, simulating the evolution of (typically isolated) massive binaries. Such simulations appear highly dependent on their adopted initial model parameters, e.g., initial binary fractions, mass ratios, orbital periods, and whether the simulation code includes mechanisms such as companion mass exchange or N-body dynamical interactions. Assuming an initial binary fraction of 80%, De Donder et al. (1997) found that 5–8% of O stars have runaway velocities $>30 \text{ km s}^{-1}$, and fewer than one-third of those runaway systems are binaries. Modeling only binary systems, Eldridge et al. (2011) found a runaway fraction of approximately 5% for O stars and slightly lower for B stars. Renzo et al. (2019) and Evans et al. (2020) modeled the evolution of isolated binary systems and found BSS-induced O star runaway fractions of $0.5^{+1.0}_{-0.4}\%$ and 0.5–2.0%, respectively. It should be noted that De Donder et al. (1997), Renzo et al. (2019), and Evans et al. (2020) do not consider the additional effect of dynamical ejections in their studies, focusing instead on isolated systems which likely contributes to their lower runaway fractions. Eldridge et al. (2011) acknowledged the likelihood that the DES contributes to the runaway population but predicted only modest increases in the runaway fraction over their strictly BSS predictions.

N-body simulations of stellar clusters predict that dynamically ejected runaways comprise a few percent of the general runaway O star population, similar to the contribution of the BSS. Poveda et al. (1967) modeled 5- and 6-body star clusters analytically and found that 2–17% of stars were ejected with velocities in excess of 35 km s^{-1} . Using N-body simulations of $10^{3.5} M_{\odot}$ and $10^{4.0} M_{\odot}$ stellar clusters, Oh et al. (2015) found about 30% of the ejected O stars achieve runaway velocities, producing a runaway fraction of 5% along all O stars. One of the few studies that

approaches the observed rate of runaways is the DES simulations of Perets & Šubr (2012) that predicted O runaway fractions of 5–20% and B-star runaway fractions of one-third to one-sixth that of the O star fraction.

It appears likely that both the BSS and DES contribute to the population of runaways. Indeed, some observational studies have identified runaway star candidates from clusters that are too young to have experienced their first supernova (e.g., Gvaramadze & Bomans 2008; Roman-Lopes 2013; Drew et al. 2018) making DES the only likely mechanism for producing these systems. Similarly, studies have identified high-proper-motion star+pulsar pairs with anti-parallel velocity vectors that suggest a common co-located origin, making them probable BSS-generated runaways (Hoogerwerf et al. 2000, 2001). Given that each mechanism generally produces runaway fractions of a few to several percent in simulations, combinations of the two mechanisms can only reproduce the low end of the observed runaway fractions, i.e., $<10\%$.

1.3. Goals of this Investigation

Here and Paper I we present the results of complementary studies to Peri et al. (2012), Peri et al. (2015), and Bodensteiner et al. (2018). Whereas those works began with catalogs of runaways and bright OBA stars, respectively, and searched for SBNe, we begin with the comprehensive K16 and supplementary Jayasinghe et al. (2019) catalogs of SBNe to determine their spectral types (Paper I) and kinematic properties (this work). With the high-quality measurements from the Gaia Early Data Release 3 (EDR3) (Gaia Collaboration et al. 2016b, 2018), it is possible to locate individual stars within the Galactic Plane to distances of nearly 8 kpc, greatly extending the accessible volume over previous stellar catalogs such as Hipparcos (van Leeuwen 2007) or Tycho-2 Høg et al. (2000). Previous measurements of the velocities of SBNe (van Buren et al. 1995; Bodensteiner et al. 2018) have measured proper motions without accounting for the Galactic rotation curve and often without correcting for solar peculiar motion (e.g., K16). While this is reasonable approximation when within the solar neighborhood, at distances of $>\text{few}$ kpc these corrections can be on the order of $10\text{--}30 \text{ km s}^{-1}$, similar to the runaway velocity threshold. In this work, we account for both the solar peculiar motion and the expected contribution of the Galactic rotation curve to calculate peculiar velocities within each star’s local standard of rest.

The majority of stars in the K16 catalog lack radial velocity measurements, precluding the calculation of true 3D peculiar motions. However, simulations of SBNe suggest that their arcuate shapes become increasingly reniform (circular) as the inclination angle increases beyond $\approx 45^\circ$ from transverse (Acreman et al. 2016; Meyer et al. 2016). As SBNe in the K16 catalog were identified on the basis of an arcuate morphology, this suggests that, if the star-ISM differential is created by the stellar peculiar velocity, the largest components of the peculiar velocity will be transverse and not radial. For this reason we adopt and defend the proposition that the two-dimensional peculiar velocity (v_{2D}) calculated from proper motions is a reasonable approximation of the full three-dimensional velocity (v_{3D}) for most SBN central stars.

In this work, we calculate v_{2D} for a sample of SBN central stars and a comparison sample of O stars from Galactic O-Star Catalog (Maíz Apellániz et al. 2013, 2016, GOSC) to determine their velocity distribution and runaway fractions. As a comparison sample, the GOSC contain massive stars earlier than B0 selected for completeness without regard to other properties, whereas the SBN sample is selected on the basis of infrared nebular morphology. Furthermore, the GOSC contains exclusively O stars while the SBN sample contains both O and early B stars—predominantly the latter. If the kinematic properties of O and early B stars differ systematically (e.g., as suggested by Kobulnicky et al. (2016) and Banyard et al. (2022) with regard to O stars having a higher multiplicity fraction than B stars), then the comparisons between the SBN and GOSC samples may be regarded as approximate but imperfect.

Our goals include understanding the origins of runaway stars, the physical mechanisms responsible for production of SBNe, and the role of multiplicity among SBN stars and O stars. If the SBN central stars show an excess of runaways relative to a general O star sample, this would support the idea that stellar peculiar velocities are responsible for the star-ISM velocity differential. However, if the peculiar velocities are the same as the general O-star population, this may indicate that either “*in situ*” shocks comprise a larger portion of the SBNe population or that ISM density is a more important factor in the formation of an SBNe than the velocity differential. If runaway stars are predominantly single relative to the field O population then the BSS mechanism is the favored one. However, if runaways are commonly multiple-star systems, then the DES mechanism must be responsible for their large velocities.

Section 2 describes the selection of sample sources, the methods and assumptions of the kinematic computations, and spectroscopic reduction techniques for GOSC runaway O stars and SBN central stars observed. Section 3 presents results on the GOSC O-star runaway comparison sample, including the distribution of v_{2D} , runaway fraction, and

multiplicity fraction for a subsample of 455 GOSC sources. Section 4 presents two-dimensional and three-dimensional velocities of the SBN central stars sample, runaway fractions, and the distribution of alignments between the stars’ velocities and the orientation of their nebulae. In Section 5 we conclude with a discussion of these results and implications for production of SBNe and runaway stars.

2. KINEMATIC ANALYSIS AND NEW SPECTROSCOPIC DATA

2.1. Source Selection

The stellar sources for this work were selected from the K16 catalog of 709 morphologically identified SBNe candidates and their central stars, supplemented by an additional¹ 187 citizen-science-identified stars from Jayasinghe et al. (2019). We extracted *Gaia* EDR3 astrometric quantities for these 896 sources as matched by position using a 1.5'' search radius—twice the angular resolution of the mid-IR images that comprise the search dataset—from the position of the mid-infrared point source identified as the probable central star of each nebula. Positional matching resulted in 797 bowshock central stars having a viable EDR3 counterpart. Those without a match are likely objects where the central star is too faint at optical wavelengths to appear in the EDR3. In 19 instances positional matching resulted in two candidate central stars. For the majority of such cases the ambiguity was resolved by selecting the source with the optical magnitude most consistent with the infrared-identified point source IR magnitudes. Of the stars having an EDR3 entry, only 582 have a physically meaningful positive parallax. We removed 78 stars having a renormalized unit weight error parameter (Lindegren et al. 2018, RUWE) >1.4 , as these have astrometric solutions showing larger-than-expected residuals—possibly as a consequence of binarity—resulting in less reliable proper motions. Finally, we retained only the stars having parallax and proper motion measurement:error ratios greater than 4:1, leaving 267 objects having well-measured astrometric parameters. The 16th/50th/84th percentiles of the *Gaia* G-band magnitudes of selected stars are 9.5/12.6/14.8, so the majority of the sources are considered bright targets.

We created a field O star (non-bowshock) comparison sample from the 590-source GOSC, as compiled in Maíz Apellániz et al. (2016) using the same selection criteria as for the SBN central stars, resulting in 455 O stars comprising the GOSC comparison sample.

Figure 1 plots the Galactic locations of the 455 GOSC O stars (*blue x’s*) and 267 SBN central stars (*red dots*) in each sample using a polar representation with the Sun at center and Galactic Center toward right. The vast majority of the SBN central stars lie in the inner Galaxy, with a comparable number in the first quadrant (112 objects) and fourth quadrant (117 objects). Nearly all SBN objects lie within 1° of the Galactic Plane. The mean distance is larger for SBN central stars (3.3 kpc) than for GOSC O stars (2.3 kpc), a likely consequence of the infrared selection criteria for the former and optical selection criteria for the latter.

2.2. Kinematic Calculations

We computed the Galactic position and peculiar velocity (v_{2D} from the two proper motion components) for each source relative to its local standard of rest based upon the EDR3 proper motions and parallax-based distances. Uncertainties on parallaxes and proper motions are, on average, factors of 3–5 smaller in the EDR3 compared to the earlier DR2 dataset. We adopted inverse parallax values for the distances. The calculation of velocities is based upon the matrix equations of Johnson & Soderblom (1987) in conjunction with an adopted solar motion relative to the Local Standard of Rest (LSR) and an adopted Galactic rotation curve. For a complete description of this technique and the associated matrix transformations, see Appendix A of Randall et al. (2015). To transform from equatorial to Galactic coordinates, we adopted the Reid & Brunthaler (2004) Galactic Center coordinates ($\alpha_{GC} = 17^h:45^m:37\rlap{.}^s224$, $\delta_{GC} = -28^\circ:56':10\rlap{.}''23$) and Galactic North Pole coordinates ($\alpha_{GNP} = 12^h:51^m:26\rlap{.}^s282$, $\delta_{GNP} = 27^\circ:07':42\rlap{.}''01$). We adopted a Solar Galactocentric distance of 8.15 kpc (Reid et al. 2019) and the Irrgang et al. (2013) Model II Galactic rotation curve. The choice of rotation curve makes very little difference to the calculated velocities because all modern rotation curves are nearly flat within a few kpc of the Sun where most of our sample stars lie. The calculation of peculiar stellar velocities, however, is somewhat sensitive to the adopted Solar motion relative to the LSR. We tried both the solar peculiar motions of Schönrich et al. (2010), $[U_\odot, V_\odot, W_\odot] = [11.1 \pm 1.2, 12.2 \pm 2.1, 7.2 \pm 0.6]$ km s $^{-1}$ and those of Ding et al. (2019) which are based on *Gaia* DR2 stellar kinematics, $[U_\odot, V_\odot, W_\odot] = [8.63 \pm 0.64, 4.76 \pm 0.49, 7.26 \pm 0.36]$ km s $^{-1}$. We found neither to be satisfactory. Motivated by the reasons and analysis described in the Appendix we

¹ The objects were selected by senior author H.A.K. using the same morphological criteria as in K16 from among the 311 Jayasinghe et al. (2019) additional candidate stars not contained in the K16 catalog.

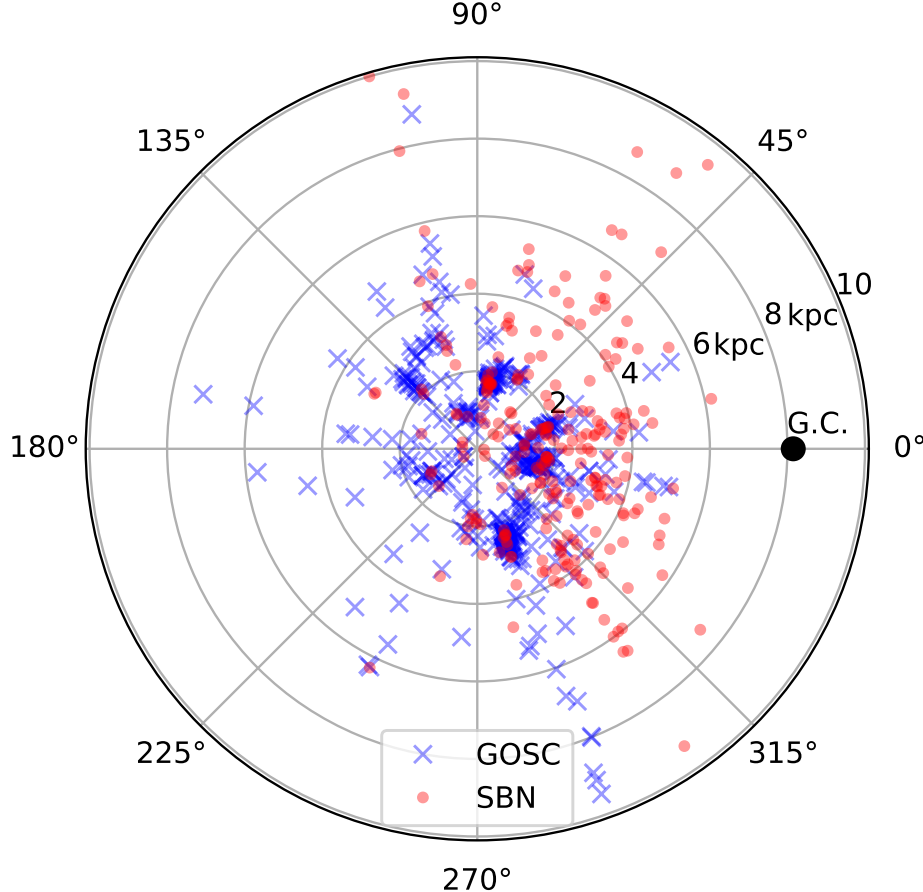


Figure 1. Polar representation of the Galactic locations of GOSC O stars (blue *x*'s) and SBN central stars (red dots), with the Sun at center and Galactic Center toward the right.

adopted $[U_{\odot}, V_{\odot}, W_{\odot}] = [5.5 \pm 1, 7.5 \pm 1, 4.5 \pm 1] \text{ km s}^{-1}$. These values are within the uncertainties and plausible ranges of many historical determinations (e.g., see summary table of Ding et al. 2019).

We estimated the uncertainties on the peculiar velocities using a 1000-iteration Monte Carlo analysis, taking into account the EDR3 uncertainties on parallax and the two proper motion components, along with the uncertainties on the solar motion relative to the local standard of rest. This method produces distributions of peculiar velocities in U , V , and W . We then added in quadrature the uncertainties of each peculiar velocity distribution to determine the uncertainty on v_{2D} . We did not consider systematic uncertainties on the EDR3 motions, as these are estimated to be $\lesssim 0.004 \text{ mas yr}^{-1}$, negligible compared to the random uncertainties and small compared to the earlier Gaia DR2 systematic uncertainty of $\sim 0.010 \text{ mas yr}^{-1}$ (Gaia Collaboration et al. 2021). Likewise, the systematic error on the EDR3 parallaxes is estimated at $\sim 0.010 \text{ mas}$, negligible for the purposes of this work (Lindegren et al. 2021). Uncertainties on EDR3 parallaxes may be up to a factor of two larger than the published values as a complex function of location on the sky, color, and magnitude (Lindegren et al. 2021; Maíz Apellániz et al. 2021; Cantat-Gaudin & Brandt 2021), but we do not consider these owing to the evolving understanding of *Gaia* systematics as of this writing. Proper motions of bright ($G < 13$ mag) stars may also be systematically rotated with respect to fainter targets (Cantat-Gaudin & Brandt 2021), so we performed an analysis with and without their recommended corrections using their code and concluded that these are insignificant to the conclusions of this work.

For those sources with two or more radial velocity measurements from our spectroscopic survey, we calculated a 3-dimensional peculiar velocity (v_{3D}) using the weighted mean radial velocity measurement and adopting the RMS of those measurements as the associated uncertainty. This mean is used to minimize the effects of potential radial velocity deviations from binary (or higher-order multiple) systems, both identified and unidentified.

Adding signed quantities in quadrature (i.e., the two components of proper motion) always contributes positively to the final value. We correct for this positive bias by subtracting in quadrature the velocity uncertainties (σ_i) from the calculated velocities (v_i) for each star,

$$v_i = \sqrt{v_i^2 - \sigma_i^2}. \quad (1)$$

For the selected sources with small fractional uncertainties, this bias correction is small relative to the uncorrected velocities. The median positive bias correction is 1.7 km s^{-1} for the GOSC stars and 1.8 km s^{-1} for the SBN stars. In order to test and validate our code, we replicated the [Sperauskas et al. \(2016\)](#) analysis of the peculiar motions of 1088 K-M stars in the solar neighborhood using their set of assumptions and Galactic rotation curve. The average absolute difference between their calculated peculiar velocities and ours is $1.1 \pm 1.0 \text{ km s}^{-1}$.

2.3. Spectroscopic Observations of GOSC O Stars

In addition to the optical spectra acquired previously on 84 SBN stars for Paper I, we obtained spectra of 25 stars from the GOSC, selected on the basis of having large v_{2D} (in excess of 25 km s^{-1}), high source brightness (broad range of $7.2 \lesssim V \lesssim 11.2$ mag), and positive declinations suitable for observation from the northern hemisphere. No sharp magnitude cut was applied so that the sample is not biased toward more luminous (hence, binary) stars. These sources also met the astrometric selection criteria described above. We obtained 119 new optical spectra using the Wyoming Infrared Observatory (WIRO) 2.3 meter and Apache Point Observatory (APO) 3.5 meter telescopes. Each star in this sample was observed on at least three separate nights, with thirteen stars observed more than five nights. The interval between observations varied between one and 84 days with a mean of 30 days and a median of 32 days. The mean time baseline from first to last observation was 107 days with a median of 118 days. All but one star had a minimum baseline of 57 days with 17 of the 25 stars having a baseline longer than 90 days.

We acquired 81 spectra on the nights of 2019 July 29, August 16, 28, and 19, and September 4 using the WIRO LongSlit spectrograph. Observational methodologies for WIRO spectra closely follow those described in Paper I. During each observation, sources were positioned within a $1''.2 \times 120''$ slit oriented north-south. A 2000 line mm $^{-1}$ grating yielded a spectral resolution of 1.26 \AA FWHM ($R \approx 4000$) with a spectral coverage of $5400\text{--}6800 \text{ \AA}$. Exposure times ranged from 1×30 s to 2×300 s, depending on source brightness and seeing. CuAr arc lamp exposures were taken before and after each exposure, yielding wavelength solutions with a typical RMS of 0.015 \AA , or 0.8 km s^{-1} at 5800 \AA . The wavelength calibration is estimated to be precise to 6 km s^{-1} .

We acquired 38 spectra using the Double Imaging Spectrograph (DIS) on the APO 3.5 meter telescope over seven nights: 2019 May 24, 2019 July 3 and 9, 2019 September 4 and 25, and 2019 October 22 and 29. The 1200 line mm $^{-1}$ grating of the red spectrograph arm yielded a reciprocal dispersion of $0.58 \text{ \AA pix}^{-1}$ over the $5700\text{--}6900 \text{ \AA}$ wavelength range. Depending on source brightness, exposure times ranged from 1×20 s to 2×120 s. The instrument HeNeAr arc lamp supplied wavelength calibration to an RMS of 0.06 \AA . Instrument rotation during the night produces wavelength shifts of up to 0.3 pix, which were removed using periodic HeNeAr arc lamp exposure such that the wavelength solutions are estimated to be precise to about 5 km s^{-1} .

Spectra were extracted and reduced using standard longslit techniques within IRAF ([Tody 1986](#)). Flat-fielding was performed using quartz lamp dome flats for WIRO spectra and internal quartz lamp flats for APO spectra. Where multiple spectra were taken in a single target, nightly spectra were combined into a single master spectrum yielding a final signal-to-noise ratio (SNR) of at least 65 for APO spectra and 80 for WIRO spectra in the vicinity of the stellar He I 5786 \AA line used to measure radial velocities. Final spectra were continuum normalized and Doppler corrected to the Heliocentric velocity frame. Radial velocities were extracted using the methodology described in Paper I. Briefly, the Heliocentric velocity for each spectrum was re-zeropointed by shifting it (typically $3\text{--}15 \text{ km s}^{-1}$) to place the centroids of the interstellar Na I D $\lambda\lambda 5890, 5896$ lines at the mean velocity for the ensemble of each star. Using a fitting code based around the IDL routine MPFIT [Markwardt \(2009\)](#), we measured radial velocities from each spectrum by fitting Gaussian functions to the He I 5786 \AA line. This fitting code fixed the Gaussian width and depth to the mean from the ensemble after manually rejecting outliers and solved for the best line center and uncertainty. This technique allowed us to measure robust *relative* radial velocities but, since our data lack radial velocity standards, these should not be treated as absolute radial velocities due to potential systematic offsets relative to the Heliocentric frame. We estimate any such absolute systematic effects to be small, $< 8 \text{ km s}^{-1}$, based on calibrations of other surveys using the same instrument ([Kobulnicky et al. 2014](#)).

3. GOSC COMPARISON SAMPLE RESULTS

3.1. Runaway Fraction of the General O Star Population

Figure 2 presents a histogram of the distribution of v_{2D} for the 455 GOSC stars, using a bin width of 2.5 km s^{-1} . Vertical dashed lines mark the two fiducial thresholds for runaways at $v_{2D} > 25 \text{ km s}^{-1}$ and $v_{2D} > 30 \text{ km s}^{-1}$, respectively. Five systems lie off the right edge of the plot at $v_{2D} > 100 \text{ km s}^{-1}$. The distribution in Figure 2 is similar to the peculiar tangential velocities of Tetzlaff et al. (2011, Figure 4) having a peak near 8 km s^{-1} with a long tail extending out to 100 km s^{-1} . Tetzlaff et al. (2011) do not apply a positive bias correction so their distributions may be biased to slightly larger velocities. The median/mean velocity uncertainties are $1.8/2.6 \text{ km s}^{-1}$.

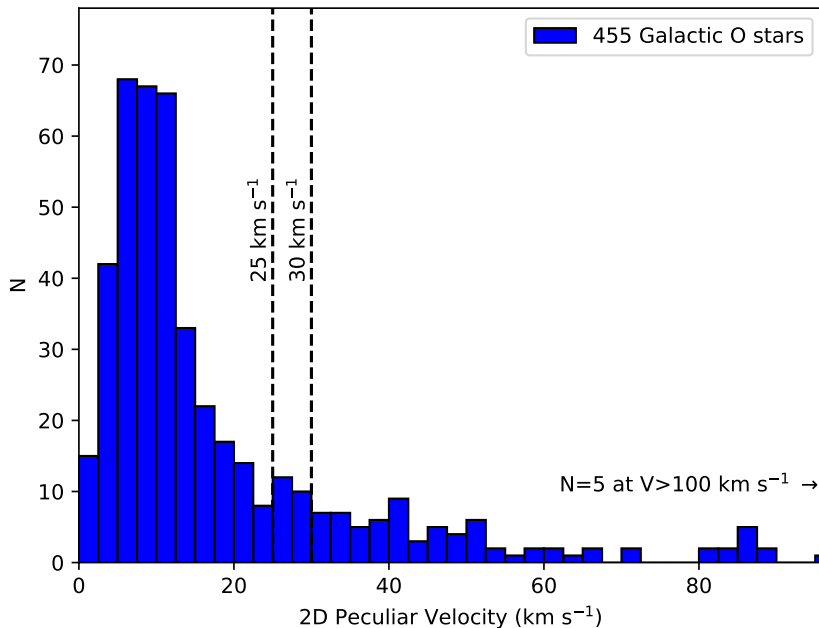


Figure 2. A histogram bias-corrected 2D peculiar velocities of 455 O stars from the Galactic O Star Catalog (Maíz Apellániz et al. 2016). Vertical dashed gray lines indicate the v_{2D} runaway thresholds of 25 km s^{-1} and 30 km s^{-1} .

Of the 455 GOSC sources, 81^{+14}_{-8} , have $v_{2D} > 30 \text{ km s}^{-1}$, yielding a runaway fraction of $16^{+3\%}_{-1\%}$. For this work, we adopt a v_{2D} runaway threshold of 25 km s^{-1} as our primary runaway star criterion, for two reasons. Tetzlaff et al. (2011) analyzed 7663 stars within 3 kpc of the Sun and found the peculiar tangential velocities (our v_{2D}) could be described by a two-component Gaussian distribution, with low- and high-velocity components peaking at 7 and 22 km s^{-1} , respectively. These low- and high-velocity distributions intersect at 20 km s^{-1} , with the low-velocity component approaching zero amplitude at $\geq 25 \text{ km s}^{-1}$. Therefore, adopting 25 km s^{-1} as our v_{2D} threshold would select only members of this high-velocity group. Furthermore, a v_{3D} threshold of 30 km s^{-1} corresponds to a v_{2D} threshold 25 km s^{-1} ($\sqrt{3/2} \approx 30/25$). After applying the positive bias correction to the data, our v_{2D} threshold of 25 km s^{-1} yields 102^{+14}_{-15} of 455 GOSC O stars as runaways ($22^{+3\%}_{-3\%}$).

Our GOSC runaway fraction is notably higher than that found by Maíz Apellániz et al. (2018) who analyzed 594 GOSC stars (including some previously unpublished stars) using Gaia DR1 proper motions. However, Maíz Apellániz et al. (2018) used a statistical analysis based on 2D proper motions corrected for solar motion, rather than a true peculiar velocity. This method was used for computational simplicity and to avoid the use of DR1 parallaxes which did not include bright sources and had large relative uncertainties. The statistical cut for their runaway candidates was empirically determined using the results of Tetzlaff et al. (2011). Maíz Apellániz et al. (2018) found 49 runaway candidate O stars out of 594 sources, yielding a runaway fraction of 8.2%, considerably lower than our $22 \pm 3\%$, as well

as lower than historical literature values for O stars. Opting to use the $v_{2D} > 30 \text{ km s}^{-1}$ fraction of $17^{+4}_{-1}\%$ reduces but does not resolve the inconsistency. One potential reason for their lower runaway rate may be their analytical method being insensitive to stellar distance. In our analysis 77 (17%) of the GOSC sources have distances greater than 3 kpc. At greater distances large transverse velocities have proportionally smaller proper motions. Because of their focus on proper motion outliers, their analysis may exclude high-peculiar-velocity stars at large distances. Of the Maíz Apellániz et al. (2018) runaway candidates our analysis recovered all 30 that met our selection criteria. Our new field O star runaway fraction of $22 \pm 3\%$ is consistent with most previous observations of O stars as outlined in Section 1, including the raw fraction found by Stone (1991) and the Blaauw (1961) O stars, but substantially lower than the Stone (1991) corrected fractions of 46% and lower than the 55% reported by de Wit et al. (2005).

3.2. Multiplicity Fraction of Runaway GOSC Stars

Table 1 lists the computed stellar kinematic properties for each of the 25 spectroscopically studied GOSC runaway candidates. Columns 1 and 2 list the GOSC catalog identification number and a common alias, respectively. Column 3 is the EDR3 RUWE. Columns 4 and 5 are the calculated v_{2D} and 1σ uncertainty. Column 6 is the mean Heliocentric radial velocity of the 3–6 individual measurements, column 7 is the average velocity uncertainty, and column 8 is the RMS of the 3–6 radial velocity measurements. Column 9 gives probability $P(\chi^2, \nu)$ for each star’s set of radial velocities being consistent with the null hypothesis (no velocity variability) using a chi-squared test with ν degrees of freedom, where ν is the number of radial velocity measurements minus one. Sources with $P(\chi^2, \nu) < 0.05$ are inconsistent with the null hypothesis of a single-star system and are interpreted as candidate multiple-star systems. Column 10 lists the spectral type and luminosity class from the literature, and column 10 gives the dates of observation for each star in a modified Heliocentric Julian Date format (HJD–2,458,000).

Figure 3 displays a histogram comparing the distributions of $P(\chi^2, \nu)$ for the 25 spectroscopically studied GOSC O stars and the 72 SBN central stars having multi-epoch radial velocity data presented in Paper I. The distributions of $P(\chi^2, \nu)$ are similar for the two populations, showing a roughly flat distribution as expected for a population of single-star systems but with a sharp peak at $P(\chi^2, \nu) < 0.05$ indicating a population of candidate multiple-star systems. Of the 25 GOSC systems, 14 ($56 \pm 16\%$) have $P(\chi^2, \nu) < 0.05$ compared to 27 of the 72 SBN central stars ($38 \pm 6\%$). If we were to consider only the 52 SBN stars meeting our astrometric selection criteria, then 16 ($31 \pm 7\%$) have $P(\chi^2, \nu) < 0.05$. Assuming the average occupancy of those bins with $P(\chi^2, \nu) > 0.05$ to be an estimate of the false positive rate for each sample yields corrected multiplicity numbers (fractions) of 13.4 GOSC stars ($53 \pm 14\%$) and 25.6 SBN central stars ($36 \pm 6\%$). If we consider only the O stars among the SBN central stars, 3 of 8 ($38 \pm 22\%$) show evidence of multiplicity. These results show that both the full OB-star SBN sample and O-star SBN sample are consistent with the runaway GOSC O-star multiplicity fraction within 1σ . The apparent multiplicity fraction of the GOSC and SBN samples are formally consistent, despite the fact that early B stars dominate the SBN sample (Chick et al. 2020), and B stars have been shown to exhibit a lower multiplicity fraction than O stars (Kobulnicky et al. 2014; Banyard et al. 2022). This bias should augment the disparity in spectral type between the samples. The consonance between SBN subsamples suggests that SBN central stars, despite consisting mostly of early B stars, may have larger multiplicity fractions than GOSC O stars. Or, this result could be interpreted to mean that binary systems are more effective in generating observable stellar bow shock nebulae, since the SBN sample is constructed exclusively by the presence of these nebular infrared features.

We considered the possibility that quasi-periodic line profile variations attributed to non-radial pulsational modes and/or stochastic atmospheric fluctuations among early type stars (rather than multiplicity) produce some of the observed variability and artificially inflate the multiplicity fraction of the GOSC sample. Fullerton et al. (1996) found that 23 of 30 O stars—and all of the supergiants in their sample—exhibited significant line profile variations in resolution $R \approx 20,000$ – $30,000$ optical spectra. Some of these would be large enough to mimic the signature of binarity seen in our $R=4000$ spectra. However, in a spectroscopic survey of 128 O and early B stars that yielded orbital solutions for 48 systems using at least 12 observations per system, only six stars were found to exhibit aperiodic line variations attributed to atmospheric effects (Kobulnicky et al. 2014). All six were supergiants. Among the present sample, 7 of the 14 GOSC stars showing velocity variability are supergiants. If we conservatively suspect all of the supergiants of being dominated by pulsational variations and remove them, this leaves 7 of 25 (28%) as multiple-star candidates. A more modest correction based on the Kobulnicky et al. (2014) survey suggests removing 2–3 velocity-variable supergiants as potential contaminants. These considerations lead us to adopt a *revised multiplicity fraction of > 28 – 48% for GOSC runaway O stars*.

All of these fractions should be considered *minimum* multiplicity fractions considering the short observational time baseline for the GOSC spectroscopic observations. The data on the SBN central stars presented in Paper I, with its longer observational time baselines, was able to identify all five previously recognized spectroscopic binary sources. Among the GOSC spectroscopic sample, five stars (GOSC IDs 27, 206, 234, 340, 365) are identified in the literature as spectroscopic binaries, primarily by Pourbaix et al. (2004). Our spectroscopic program identified three of these (27, 206, and 365) as having $P(\chi^2, \nu) < 0.05$ but did not identify the two other literature binaries. GOSC 340 (HD 192281) was originally identified as a binary system by Barannikov (1993) with a period of 5.48 days and a semi-amplitude of $16.8 \pm 2.4 \text{ km s}^{-1}$ (though Maíz Apellániz et al. (2019) note this has not been subsequently confirmed). The average velocity uncertainty for this source in our dataset is 13 km s^{-1} , of a similar magnitude as the semi-amplitude. The orbital period of GOSC 234 (HD 15137) is 28.6 ± 0.4 days McSwain et al. (2007). The irregular observational cadence of our study was 56.0, 1.0, and 60.7 days between observations, approximately two periods. This unfortunate alignment of cadence and orbital phase explains why our data do not reveal its multiplicity. Including these two literature binaries would raise the raw (uncorrected for line profile variability contamination) multiplicity fraction of our GOSC sample to 16 out of 25 sources—64%—comparable to multiplicity fractions of other OB star samples (Kobulnicky et al. 2014; Banyard et al. 2022). Our data reinforce the conclusion that multiple-star systems are common, not just among OB stars in general, but among high-velocity runaways as well.

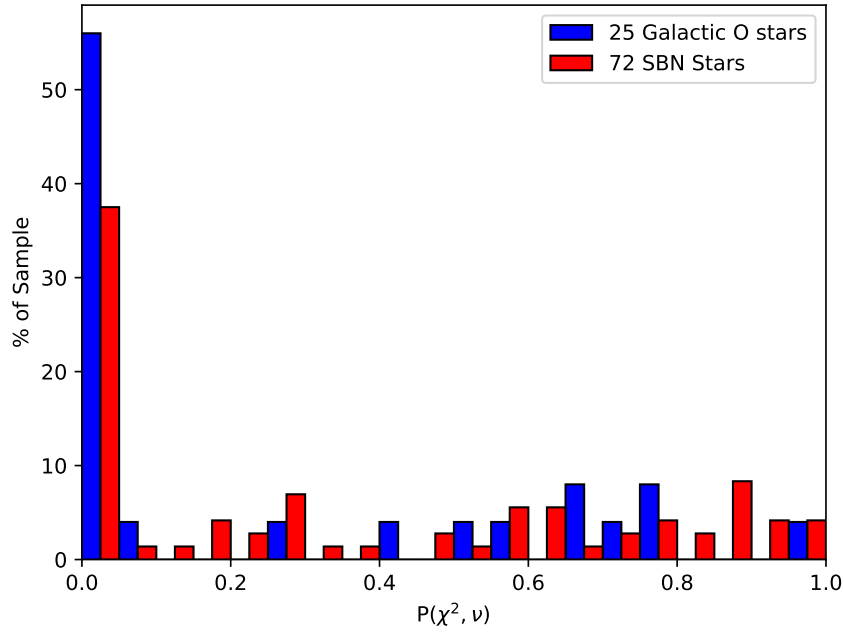


Figure 3. A histogram chi-squared probability distribution for velocities of 25 O stars from the Galactic O Star Catalog and 72 central stars of bowshock nebulae.

4. SBN CENTRAL STAR SAMPLE ANALYSIS

4.1. Kinematics of the Central Stars of Stellar Bowshock Nebulae

We divided the SBN central stars that met our astrometric selection criteria into three subsamples. The first group is the “Multiple-Star Candidates”: 16 sources, selected on the basis of having $P(\chi^2, \nu) < 0.05$. The second group is the “Single Star Candidates”: 36 sources having $P(\chi^2, \nu) \geq 0.05$. There are likely to be multiple-star systems in this group that were not identified in our radial velocity survey. However, the fraction of binaries in this sample will be lower than a typical SBN central star sample. The third group, termed “Group 3”, consists of the 215 sources that met our

astrometric selection criteria but do not have measured radial velocities. This sample is likely the most representative of SBN sources in general based upon the multiplicity cuts for the first two groups.

Table 2 provides identifications and tabulated astrometric data for the 267 SBN central stars meeting our astrometric selection criteria. Column 1 is either the K16 catalog identification number from Kobulnicky et al. (2016, numbers 1–709) or an identification index that includes the 187 additional stars drawn from Jayasinghe et al. (2019, numbers 710–896). Column 2 is a common alias for the star. Columns 3 and 4 are the right ascension and declination of the star, in degrees. Column 5 is the EDR3 ID number. Column 6 gives the *Gaia* G magnitude. Column 7 is the environment class from K16 specifying the local environment of the nebula as isolated (I; 155 instances), facing an H II region (FH; 50 instances), within an H II region (H, 30 instances), or facing a bright-rimmed cloud (FB, 30 instances). An FB designation often entails an H designation, so some objects have a compound environment class (e.g., FB/H). Columns 8 and 9 give the EDR3 parallax and uncertainty, in milliarcsec. Columns 10–13 give the EDR3 proper motion in right ascension and declination, in milliarcsec yr⁻¹, and their associated uncertainties. Column 14 is a code designating each star as part of the Multiple Star Candidates group (1), Single Star Candidates group (2), or the Group 3 (3). Column 15 is the spectral type, either from Paper I where sources were classified into three broad categories O/OB/B, or from the literature, in which case the spectral type and luminosity class is enclosed in parentheses. Column 16 lists the literature reference for the spectral classifications in parentheses.

The literature spectral types of Table 2 reinforce the conclusions of Paper I that the central stars of SBNe are predominantly OB spectral types. Of the 141 sources with spectral types, 136 are OB stars, three are M stars (possibly the evolved descendants of massive stars), one is a carbon star, and one is a K star. As part of this work, we examined the Wide Field Infrared Explorer (WISE) and *Spitzer Space Telescope* archival images to re-evaluate local environments of the SBN central stars using the criteria of K16. We cannot determine that the arcuate ISM structures are co-distant with the SBN central stars, only that these structures are co-located on the sky. For the majority of sources (65%), we affirmed the environment class of K16. Of the sources for which we reassign the local environment class, 13 of 56 resulted from changing identifications within complicated regions (e.g., updating a source from an H to an FB where the rim of an interstellar bubble was prominent at 8.0 μ m). Nearly half, 24 of 56, involved updating sources from I to FB or FH. These sources were largely 5–15 arcmin from the associated H II region or bright-rimmed cloud, many without sharp boundaries. The remaining 19 sources we reassigned the environment class from I to H, where these stars and H II regions appear at the edge of WISE ATLAS tiles. For the 50 sources in Table 2 drawn from the extended bowshock candidate list of Jayasinghe et al. (2019), the listed environmental classes are new to this work.

Table 3 lists kinematic measurements for the SBN central stars. Column 1 is the identification number, as in Table 2. Columns 2 and 3 give the calculated v_{2D} and associated uncertainty in km s⁻¹. Where radial velocities were measured for the Multiple Star Candidates and Single Star Candidates, Columns 4 and 5 provide the calculated v_{3D} and associated uncertainty in km s⁻¹. The largest source of uncertainty in the v_{2D} calculations is the distance uncertainty arising from the linear dependence of each velocity component on distance. The uncertainties on the angular proper motions, σ_{μ_α} and σ_{μ_δ} , average <1%, whereas the mean parallax uncertainty is 8%, thereby constituting the largest source of error on v_{2D} . Uncertainties on v_{3D} will always be larger than the uncertainties of v_{2D} due to the additional uncertainty term from the radial velocity measurement. For the multiple-star systems, this additional uncertainty may be significant, ≥ 6 km s⁻¹ as an observational minimum to as much as 50 km s⁻¹ for some binary systems where the systemic radial velocity is poorly constrained from just a few measurements. Column 6 lists the morphological position angle (PA_m) from the central star to the apex of the SBN, in degrees from North toward East in Equatorial coordinates, as tabulated in K16. This position angle was measured by eye based upon *Spitzer Space Telescope* 24 μ m and WISE 22 μ m archival images and carries an estimated uncertainty of 8°. Columns 7 & 8 are the kinematic position angle (PA_k) of the star's v_{2D} vector and its associated uncertainty in degrees. Columns 9 & 10 give the difference between the morphological position angle and the kinematic position angle in degrees, $\Delta PA = PA_m - PA_k$, and associated uncertainty. Column 11 provides the code, as in Table 2, designating each source as part of the Multiple Star Candidate group, the Single Star Candidate group, or the Group 3 sources which lack radial velocity measurements.

Figure 4 plots the calculated v_{3D} versus v_{2D} for the 25 systems in the GOSC runaway sample (*blue symbols*) and the 52 SBN central stars having radial velocity data (*red symbols*). Circles denote multi-star candidates, while triangles denote single-star candidates. A solid black diagonal line marks the 1:1 relation where $v_{3D} = v_{2D}$ (i.e., where a source would have zero peculiar radial velocity). A dashed line marks the relationship for isotropic velocities where the

expected $v_{3D} = \sqrt{3/2} v_{2D}$. A dotted line indicates a $v_{3D}:v_{2D}$ ratio of 2:1. The majority of SBN stars, 31 of 52 (60%), lie between the solid and dotted lines and are consistent within one sigma of the dashed line, indicating that their velocities are either entirely within the plane of the sky or consistent with an isotropic velocity distribution. This agrees with the expectation that morphologically selected SBNe central stars have velocities primarily in the plane of the sky. If a star's velocity were primarily radial through a stationary ISM, the morphology of the nebula would appear more circular than arcuate (Meyer et al. 2016). For a minority of sources (40%), particularly in the low- v_{2D} regime ($\lesssim 10 \text{ km s}^{-1}$), the ratio $v_{3D}:v_{2D}$ is greater than 2. These are likely to be either unidentified binary systems or multiple-star systems with a poorly determined systemic velocity, a consequence of having only a few radial velocity measurements. One system, the SBN multiple-star candidate 346 with $v_{3D}=220 \text{ km s}^{-1}$, lies off the top left of the plot. Upon closer examination, SBN 346 appears less arcuate and less symmetric than the other sources in the K16 catalog. Given its large peculiar radial velocity of $196 \pm 9 \text{ km s}^{-1}$ and dubious nebular morphology, we reclassify this as a doubtful SBN candidate. It may be a radial velocity runaway or a multiple-star system with a poorly determined radial velocity.

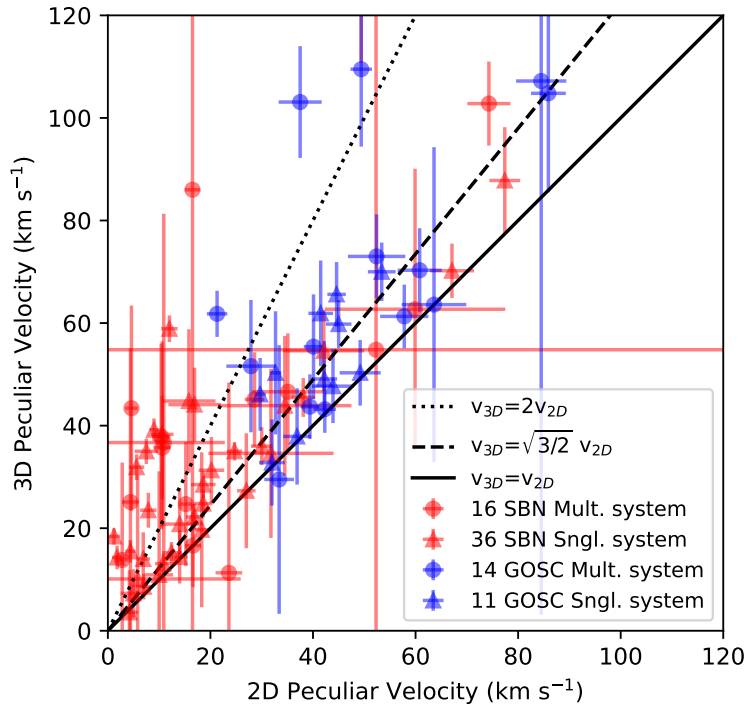


Figure 4. Three-dimensional peculiar velocity versus two-dimensional peculiar velocity for multiple star candidates (circles) and single-star candidates (triangles) from the SBN sample (red) and the GOSC comparison sample (blue). Only stars having multiple radial velocity measurements and meeting the astrometric selection criteria are shown. A solid line marks the 1:1 correspondence, while a dashed line marks the $\sqrt{3/2}:1$ relation expected for isotropic velocities in three dimensions.

For some SBN central stars the calculated v_{2D} may not be representative of the true star-ISM velocity differential if there exists a significant local flow of interstellar material. Such a local flow will be a significant factor in determining the nebular morphology and the relative star-ISM velocity, most dramatically so if the star's peculiar velocity is small. Winds from H II regions may impart local flow velocities as large as 30 km s^{-1} (Tenorio-Tagle 1979; Bodenheimer et al. 1979; Castaneda 1988). If a local flow is transverse, the star-ISM velocity differential would also be transverse creating the arcuate morphology without need for a stellar peculiar velocity. This may help explain why stars with peculiar velocities seemingly dominated by radial velocity components exhibit arcuate SBN. This class of objects would include the “in-situ” bowshock candidates where an arcuate nebula points toward a nearby H II region (e.g., our FH environment class). Of the 267 SBN objects in this sample, 50 (19%) have FH environmental classifications, meaning that a non-negligible fraction could be influenced by local ISM flows.

4.2. The Runaway Fraction of SBN Central Stars

Figure 5 presents histograms and kernel density estimates (KDEs) for the three SBN central star groups: Group 3 systems (cyan), the Single-Star Candidates (magenta), and the Multiple-Star Candidates (green). Colored curves denote the KDE for each group and the full SBN sample (*black dashed curve*). An unfilled black histogram and black solid curve designate the distribution and KDE of the 455 GOSC stars, renormalized to facilitate comparison. The KDEs for each population show a distinct peak centered near 9 km s^{-1} and a long tail out to 80 km s^{-1} and beyond. Although the KDEs suggest the Single Star Candidates may contain a high fraction of runaway stars, this may be a result of the small number of stars in that group. All SBN groups are consistent with having been drawn from the same parent population with the p-values (from K-S tests) >0.30 for all sample comparisons. However the SBN and the GOSC distributions are different at the $p=0.003$ level. This difference is mostly driven by the B stars within the SBN sample, as a comparison of just the SBN O stars with the GOSC sample results in $p=0.042$, marginally consistent with being drawn from the same population. The SBN sample is noticeably shifted toward larger velocities and has fewer objects at small velocities. The 16th/50th/84th percentile velocities of the SBN sample are $6.5/14.6/32.6 \text{ km s}^{-1}$ versus $5.6/11.4/32.6 \text{ km s}^{-1}$ for the GOSC sample. This difference could be attributed to the larger distances for the SBN stars (mean distance of 2300 pc) than the GOSC stars (mean distance of 3300 pc), since transverse velocity inferred from proper motion scales linearly with distance.

From the v_{2D} velocities of the 267 SBN central stars we identified 63^{+25}_{-18} candidate runaways with $v_{2D}>25 \text{ km s}^{-1}$. This implies a runaway fraction of $24^{+9}_{-7}\%$, nearly identical to that of the GOSC O stars.

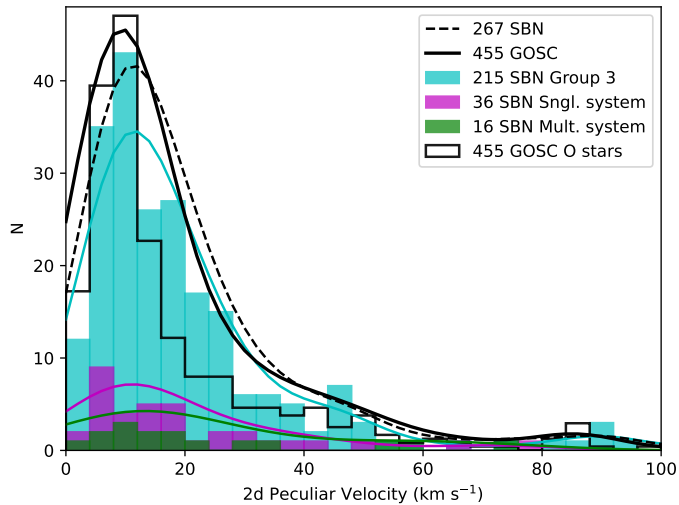


Figure 5. Histogram of v_{2D} peculiar velocities for subsamples of SBN central stars: the Multiple-Star Candidates (green), the Single-Star Candidates (magenta), and the Group 3 sample (cyan). Curves denote Gaussian probability density estimates for each subsample of SBN stars and for the entire sample of 267 SBN central stars (*black dashed curve*) and the GOSC sample (*black solid curve*). The distributions of the SBN sample and the GOSC O-star sample are statistically different.

Among the 142 stars with spectral classifications from the literature or our work (Paper I), 43 (30%) are O stars, 61 (43%) are early B stars, with the remainder (26%) being indeterminate OB stellar types on the O9/B0 boundary (other than the six late-type stars F–M). Of the 43 O stars, 12^{+2}_{-1} have $v_{2D}>25 \text{ km s}^{-1}$ ($28^{+4}_{-2}\%$). This O-star runaway fraction is larger than the $22\pm3\%$ observed among the GOSC stars and is consistent with the high end of the observed O star runaway fractions (e.g., Blaauw 1961; Stone 1991; Oh et al. 2015). Among the 61 B stars, 16^{+4}_{-1} ($26^{+7}_{-2}\%$) are runaway star candidates, much larger than the 2% B star runaway fractions measured by Blaauw (1961) and Gies & Bolton (1986). For the sample SBN central stars, it appears that O and B stars have similar runaway fractions. Among the 16 Multiple-Star Candidates 3^{+2}_{-1} ($18^{+18}_{-12}\%$) has $v_{2D}>25 \text{ km s}^{-1}$, whereas 9^{+2}_{-2} ($25^{+5}_{-6}\%$) of the 36 Single

Star Candidates are runaway stars. Within the Poisson uncertainties, multiple-star systems and candidate single-star systems have similar runaway fractions.

4.3. Morphological and Kinematic Position Angles

We used the computed Δ_{PA} parameter—the difference between morphological and kinematic position angles—to assess the degree of alignment between the SBN morphological position angles and the stars' peculiar velocity vectors. Figure 6 presents a histogram of the Δ_{PA} distribution for the 267 SBN central stars, using bin widths of 10° . The Figure shows a peak near $\Delta_{PA}=0^\circ$, indicating strong alignment between the morphological axes of the SBN and the peculiar motion vectors. This peak is present regardless of the choice of Solar peculiar motions (see Appendix), but is more pronounced by about 50% when the adopted $[U_\odot, V_\odot, W_\odot]$ values are used. There is a broad tail to either side, with some sources showing anti-alignment ($\Delta_{PA}=\pm 180^\circ$). The distribution can be approximated by two hypothetical populations: a highly aligned population centered near 0° having a Gaussian width of $\sigma=25^\circ$ (dashed curve) and a random (non-aligned) population. The solid black curve depicts the sum of these two components. The “highly aligned population” comprises 31% of the sample, while the “random population” comprises 69%. The overall distribution is similar to that presented in K16 (Figure 12) but contains more sources, uses better astrometric data, and corrects for solar motion relative to the Local Standard of Rest.

The two populations identified on the basis of Figure 6 suggest that, in a minority of cases, the stellar peculiar velocities are responsible for shaping the orientation of the nebulae. In a majority of cases, there is considerable dispersion between the star's velocity vector and the morphological axis of the nebulae. This suggests that local environmental factors, such as local ISM flows or the proximity to an H II region or bright-rimmed cloud undergoing photoevaporation—rather than the stellar motion—dominates the formation of the nebulae in most instances. Notably, in about 12% of the sources, $|\Delta_{PA}|>100^\circ$, indicating anti-alignment between morphological and kinematic position angles. Such anti-alignment could occur in cases where an OB star is ejected from a nearby H II region and an outflow from that H II region impinges upon the star.

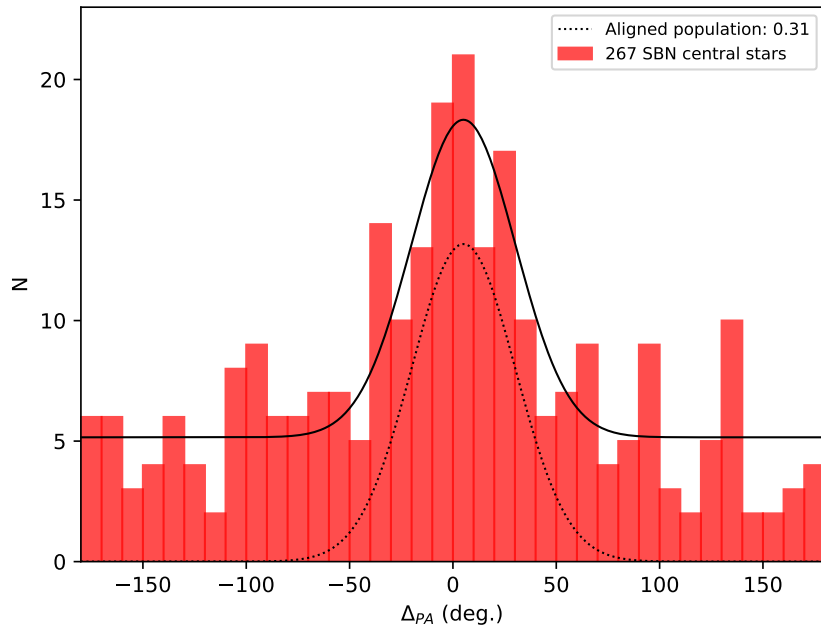


Figure 6. Histogram of Δ_{PA} , the difference between the morphological position angle of the arcuate nebulae and the position angle of the central star's projected peculiar velocities. The distribution is well approximated by the sum (*solid curve*) of a Gaussian component representing a highly aligned population (*dashed curve*) and a random (flat, non-aligned) component.

Figure 7 plots a histogram of Δ_{PA} color coded by environment class, with solid black bars denoting stars in isolated environments (I), blue hatched bars denoting stars either inside H II regions (H) or facing bright-rimmed clouds (FB), and red transparent bars depicting stars facing toward nearby H II regions. Bin widths are twice as large as in Figure 6 owing to the smaller numbers of sources in the latter two groups. We merge the H and FB designations, as stars inside H II regions often face bright rims lining those cavities and may encounter similar photoevaporative flows. The largest group, the isolated stars (I), shows a similar distribution of Δ_{PA} to the general population in Figure 6. Of the 155 stars in isolated environments, 115 (74%) are highly aligned, having $|\Delta_{PA}| < 45^\circ$. The two remaining groups, H/FB and FH, both have flatter distributions with small, but not statistically significant overdensities near $\Delta_{PA} = 0^\circ$. Assessed another way, the Pearson correlation coefficient between PA_m and PA_k is $r=0.37$ ($p=10^{-6}$) for the 155 environment class I stars, confirming the strong correlation. The 62 FB/H environment class stars have $r=0.11$ and $p=0.36$, indicating a weak or no significant correlation. The 50 environment class FH stars also show no correlation ($r=0.04$, $p=0.75$). The weak or non-existent correlation for FB/H stars is unsurprising, as we would expect significant small-scale flows in the proximity of bright rimmed clouds and bubbles where photoevaporative flows are common and significant relative to the peculiar velocity of the stars. The lack of correlation for FH stars is also unsurprising. We would also expect flows emanating from H II regions—at velocities that may dominate the relative star-ISM differential in cases where the star’s velocity is small. Finally, we stress that our environmental classifications are an imprecise characterization of the stars’ true local conditions, based only on angular separations from prominent infrared features. A more quantitative analysis comparing SNe three-dimensional Galactic positions with those of OB stars and H II regions would improve the reliability of the environmental classifications. Such an effort should now be possible but is beyond the scope of this work.

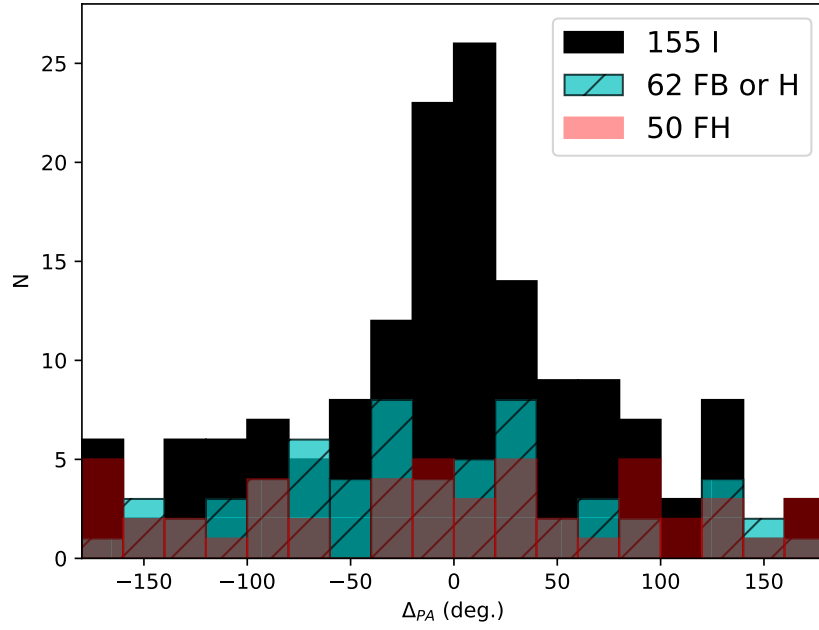


Figure 7. Histogram of Δ_{PA} , with systems color coded by local environment class. Isolated systems peak strongly near zero, indicating alignment between morphological and kinematic vectors. FB/H and FH stars have a nearly flat distribution.

Figure 8 plots Δ_{PA} versus v_{2D} for the SBN sample. Black symbols and error bars mark isolated stars (I), cyan symbols mark stars inside H II and facing bright-rimmed clouds (H/FB), and red symbols mark stars with SBN facing nearby H II regions. Numerical labels identify some of the highest velocity stars. A vertical magenta bar delineates the runaway threshold of 25 km s^{-1} . The gray shaded rectangular region marks the regime where morphological positions angles are highly aligned with the kinematic vectors ($|\Delta_{PA}| < 45^\circ$) and $v_{2D} > 25 \text{ km s}^{-1}$. With few exceptions, the stars

with the largest velocities also have the smallest Δ_{PA} , falling within the shaded region. Forty-four of the 155 isolated stars ($28\pm4\%$), eight of the 62 FB/H stars ($13\pm5\%$), and ten of the 50 FH stars ($20\pm6\%$) are runaways. Thirty-eight of the 63 runaway stars (80%) show strong alignment (within 45°) between their morphological and kinematic position angles. Among stars with projected velocities $<25 \text{ km s}^{-1}$, there is a large dispersion in Δ_{PA} . Evidently factors other than peculiar velocity determine Δ_{PA} for these nebulae, such as local ISM flows that are on the order of the $\approx 10 \text{ km s}^{-1}$ peculiar velocities measured for this population. Other factors may include density inhomogeneities in the vicinities of spiral arms, molecular clouds, or star clusters that create departures from the smooth circular Galactic rotation curve assumed in computing v_{2D} .

Among the runaways a few stars show dramatic misalignment, having $\Delta_{PA}>120^\circ$. Star 303 (labeled in Figure 8) is among the most distant in the sample ($d>10 \text{ kpc}$ at Galactic longitude $\ell=60^\circ$), giving it a parallax uncertainty that results in a very large uncertainty on v_{2D} ($\sigma_{v_{2D}} = 68 \text{ km s}^{-1}$). Formally, it is consistent with having a negligible (non-runaway) peculiar velocity. Star 865 ($v_{2D}=108 \text{ km s}^{-1}$) is also quite distant ($> 5 \text{ kpc}$ at $\ell=340^\circ$) but has well-measured kinematics. It appears to be confined within an interstellar cloud or bubble irradiated by an external source of illumination, so the tabulated morphological position angle probably corresponds to the direction of this radiation and not the stellar velocity vector. The nebula preceding Star 873 is compact and appears isolated from external influences; we have no good explanation for the large $\Delta_{PA}=-147^\circ$. Star 880 has a well-defined nebula and well-measured kinematics, yet its morphological orientation is nearly 180° from its projected velocity. Star 624 faces an H II region, has a velocity just above the 25 km s^{-1} threshold, and shows anti-alignment at $\Delta_{PA}=170^\circ$.

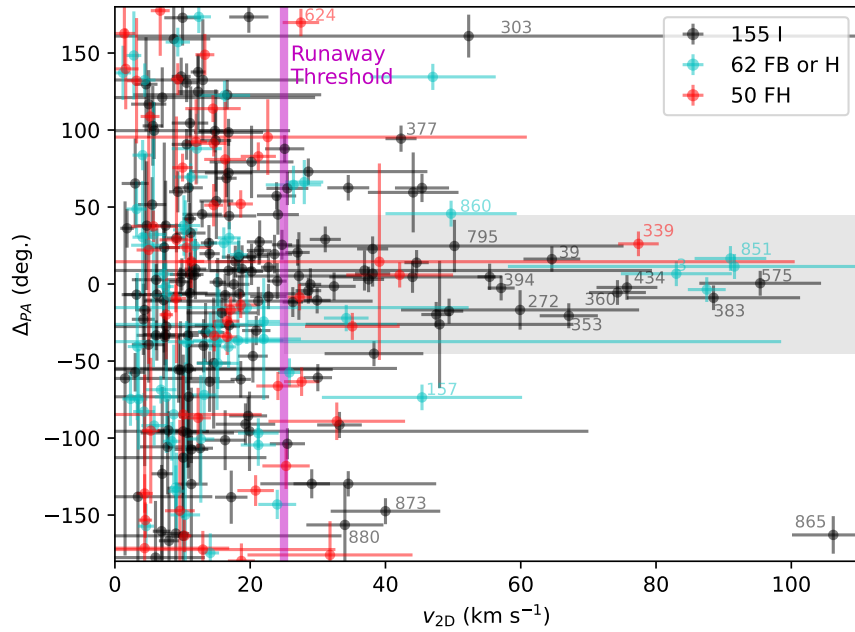


Figure 8. Δ_{PA} versus v_{2D} peculiar velocity. Colors distinguish the I, FB/H, FH environment classes. The gray shaded region marks the regime of runaway stars ($v_{2D}>25 \text{ km s}^{-1}$) that have nebular morphological position angles aligned with the central stars' velocity vectors ($|\Delta_{PA}|<45^\circ$).

5. CONCLUSIONS

The Gaia EDR3 astrometric data and new multi-epoch optical spectroscopy has allowed us to investigate the kinematic properties of a large sample of morphologically selected stellar bowshock nebulae and their central stars. Quantities of particular interest for addressing the origins of bowshock nebulae and runaway stars are the stellar peculiar velocities (both 2D and 3D), their multiplicity, as evidenced by the dispersion in radial velocity measurements, and the degree of angular alignment between the SBNe morphological axes and stellar kinematic vectors. For comparison we have computed the same quantities for a control sample of Galactic O stars. Table 4 provides a summary of key statistics derived from this study regarding runaway fractions, multiplicity, and alignment of SBN morphological and central star kinematic axes.

Based on the v_{2D} velocities the runaway fraction for SBN central stars is $24^{+9}_{-7}\%$, nearly identical to the $22^{+3}_{-3}\%$ runaway fraction for GOSC stars. The SBN runaway fraction is consistent with the high end of simulations (Oh et al. 2015) and observations (Blaauw 1961; Stone 1991), but generally larger than most estimates. The SBN sample consists primarily of early B stars, and so the runaway fractions are much larger than other estimates of B stars which lie near 2% (e.g., Blaauw 1961; Gies & Bolton 1986). We conclude that while the runaway rate of SBN central stars is likely enhanced relative to the general OB population, runaway stars do not comprise a majority fraction of SBN central stars. The median v_{2D} of our sample is 14.6 km s^{-1} , far below runaway thresholds and contrary to some common assumptions that bowshock central stars have large peculiar velocities. Both the Multiple-Star Candidates group and the Single-Star Candidate group show similar runaway fractions, indicating that the mechanism responsible for their large velocities apparently acts on binary systems with equal efficiency as single stars. This observation would seem to favor the DES (N-body interactions in clusters) over the BSS (supernova ejection) scenario.

Four of the 13 SBN runaways that have multiple spectroscopic measurements show evidence for binarity, yielding a minimum multiplicity fraction for runaways of $30^{+16}_{-15}\%$. Among the GOSC runaways in Table 1, this minimum multiplicity fraction is $>28\%$ after corrections for false positives arising from potential line profile variations caused by atmospheric pulsation. Both of these fractions are much larger than the \sim few percent proposed by most pure BSS ejection simulations (e.g., Eldridge et al. 2011; Renzo et al. 2019). DES ejection simulations predict 5–20% (e.g., Oh et al. 2015; Perets & Šubr 2012), in better agreement with—but still markedly lower than—the observed fractions for SBN central stars and Galactic O stars. If SBN central stars are representative of the population of field OB stars, as is suggested by the consonance between the samples’ multiplicity fractions and runaway fractions, this suggests that the DES contributes more heavily to the field OB population than BSS. The significant numbers of multiple systems ejected from young stellar clusters (Maíz Apellániz et al. 2022) adds evidence to this scenario. Alternatively, given the high fraction of SBN central stars in isolated environments with low peculiar velocities ($\simeq 14 \text{ km s}^{-1}$), this may provide evidence that a fraction of massive stars may form in relative isolation. However, without attempts to trace these stars back to known star forming regions and OB associations, this result is largely conjecture and begs future follow-up studies that attempt to link isolated massive stars to their birth locations.

About one-third (31%) of SBNe have morphologies that are well-aligned with the motion of their central stars—a “highly aligned population”. The majority (69%) show weak or no alignment—“the random population”. The degree of alignment increases with peculiar velocity (Figure 8). The relative lack of alignment for low-velocity stars implicates the effects of local ISM flows particularly in the vicinity of energetic H II regions. Indeed, the sources showing low degrees of alignment tend to be those facing or within H II regions or facing bright-rimmed clouds where local flows are expected to play a role (Figure 7). However, some seemingly isolated nebulae also show low levels of alignment. Given the low stellar peculiar velocities (median of 14.6 km s^{-1} for SBN stars), these flows do not need to be especially fast to influence the orientation of the nebula. The flattened distribution of Δ_{PA} for weakly aligned sources (Figure 6), may indicate that the majority of SBN central stars are isotropically distributed “walkaways” acting as the “interstellar wind vanes” (Povich et al. 2008). Enhancements in gravitational potential, such as along spiral arms, may also play a role in creating local deviations from the smooth circular Galactic rotation curve assumed in our analysis, at the level of $5\text{--}10 \text{ km s}^{-1}$. Given the consistency of SBN central star properties to those of O stars in the field, stellar bowshock nebulae are a useful infrared indicator of the presence of an OB star, particularly for identifying field populations that lie far from young clusters and OB associations.

ACKNOWLEDGMENTS

An early version of this manuscript appeared as Chapter 3 in the PhD dissertation of W.T. Chick (Chick 2020). We thank Jesús Maíz Apellániz and Doug Gies for helpful comments on an early version of this manuscript. We thank students Logan Jensen, Harrison S. Leiendecker, Jacob N. McLane, Evan Haze Nunez, Jason A. Rothenberger, and Ashley N. Piccone for taking observations that contributed to this work. Our team is grateful for support from the National Science Foundation through grant AST-1412845, AST-1411851, AST-2108347, and REU grant AST-1063146, as well as NASA through grant NNX14AR35A. This work has made use of data from the European Space Agency (ESA) mission Gaia (<https://www.cosmos.esa.int/Gaia>), processed by the Gaia Data Processing and Analysis Consortium (DPAC, <https://www.cosmos.esa.int/web/Gaia/dpac/consortium>). Funding for the DPAC has been provided by national institutions, in particular the institutions participating in the Gaia Multilateral Agreement.

Facilities: WIRO, APO

Software: IRAF (Tody 1986), astropy (Astropy Collaboration et al. 2013), SciPy (Virtanen et al. 2020)

APPENDIX

A. A NEW APPROACH TO COMPUTING LOCAL STANDARD OF REST VELOCITY

Astrometric and radial velocity measurements in the Heliocentric frame of reference require corrections for Solar motion relative to the Local Standard of Rest before conversion to a rotating Galactic reference frame. Many works have calculated $[U_\odot, V_\odot, W_\odot]$, the solar motion relative to the LSR toward Galactic center, toward the direction of prograde Galactic rotation, and toward Galactic North, respectively. A wide range of values has been reported— $U_\odot=6\text{--}12 \text{ km s}^{-1}$, $V_\odot=3\text{--}26 \text{ km s}^{-1}$, $W_\odot=5\text{--}9 \text{ km s}^{-1}$ —even as improved kinematic data, larger stellar samples, and better understandings of systematic biases by stellar age have emerged (e.g., Mayor 1974; Dehnen & Binney 1998; Bobylev & Bajkova 2007; Aumer & Binney 2009; Schönrich et al. 2010; Golubov et al. 2013; Ding et al. 2019). The sample under consideration here, OB stars, represent a young stellar population that likely suffer from some of the same biases (i.e., a low velocity dispersion relative to older populations) as discussed in these works. Our attempts to adopt recent estimates for $[U_\odot, V_\odot, W_\odot]$ (e.g., Schönrich et al. 2010; Ding et al. 2019) yielded stellar kinematic vectors that showed physically implausible trends by Galactic longitude. This led us to pursue using the SBN sample to derive a new estimate of the Solar motion parameters. Our intent was not a repudiation of other recent measurements of $[U_\odot, V_\odot, W_\odot]$, which are based on more extensive analyses of larger stellar samples, but rather an *ad hoc* measurement based on a fundamentally new approach that yields physically plausible results for the SBN OB stars. Our results turn out to be consistent with the range of other recent Solar motion velocities.

Our initial analyses using either the Schönrich et al. (2010) $[U_\odot, V_\odot, W_\odot]=[11.1, 12.2, 7.2] \text{ km s}^{-1}$ or the Ding et al. (2019) $[U_\odot, V_\odot, W_\odot]=[8.63, 4.76, 7.26] \text{ km s}^{-1}$ solar velocities produced systematic trends in stellar kinematic position angle with Galactic longitude. Using the former set of Solar velocities yielded SBN central star velocities that were systematically directed toward smaller longitudes in the first quadrant and larger longitudes in the fourth quadrant—a result that is physically implausible. Under the latter assumption the opposite systematic trend obtained—also implausible. An incorrect Solar motion vector can explain these systematic effects.

The choice of stellar population used to infer $[U_\odot, V_\odot, W_\odot]$ changes the computed values, most dramatically so with V_\odot (e.g., see discussion in Aumer & Binney 2009; Golubov et al. 2013). Young populations (OB stars) have colder kinematics (smaller velocity dispersion) than older populations which have had time to be heated within the Galactic potential. For the analyses in this work we chose to estimate an *ad hoc* solar motion using our SBN dataset itself by applying a set plausibility constraints that serve as boundary conditions for our estimation.

1. The kinematic vectors of SBN central stars should not correlate with Galactic longitude. Although our sample lies mostly in the first and fourth quadrants, their peculiar motions should have no preferred orientation by quadrant in order to be consistent with the expected isotropic velocities.
2. The dispersion between the nebular morphological position angles and the central star’s kinematic position angles should be minimized. Although one of the purposes of this work is to explore the extent to which morphological and kinematic position angles align, such an alignment is already apparent even without correction for LSR Solar motion. Taken as a whole, the sample distribution of SBN nebular position angles should be maximally consistent with the distribution of central star kinematic position angles.

Figure 9 illustrates the distributions of kinematic position angles for SBN central stars resulting from Solar motion parameters $[U_\odot, V_\odot, W_\odot]=[5.5, 7.5, 4.5] \text{ km s}^{-1}$, adopted as values that best satisfy the above boundary conditions. The upper panel plots Galactic longitude versus kinematic position angle in Galactic coordinates. Here, it is clear that the sample preferentially lies in the first and fourth Galactic quadrants with few objects in the second and third quadrants. There is no probable correlation ($p=0.36$) between longitude and position angle, as expected for isotropic stellar motions. The lower panel shows histograms of the bowshock nebular morphological position angles in Galactic coordinates (*red filled histogram*) and the central star kinematic position angles (*dashed black histogram*). A Kolmogorov-Smirnov (K-S) test shows that the two distributions have a 52% probability of being drawn from the same parent distribution. Both histograms show excesses near Galactic position angles 90° and 270° , i.e., along the Plane. A similar excess was noted for the SBN parent sample morphological position angles in Kobulnicky et al. (2016). We understand this excess to be a selection effect rather than a violation of isotropy. High-velocity OB stars having vectors

orthogonal to the Plane will traverse the ≈ 80 pc scale height (Clemens et al. 1988) of the inner disk's molecular layer even in their short lifetimes, making them less likely to generate detectable bowshock nebulae. Conversely, OB stars having velocity vectors parallel to the Plane will remain within this higher density layer longer and produce observable bowshock nebulae for a greater fraction of their lifetimes.

Our adopted $[U_\odot, V_\odot, W_\odot]$ not only provide stellar motions that pass the self-consistency checks outlined above, they also lie within the range of values obtained by other (more traditional) types of analysis, despite being grounded in a fundamentally new methodology. $U_\odot = 5.5 \text{ km s}^{-1}$ lies at the low end of—but consistent with—published ranges (see Table 1 of Ding et al. 2019, $5.5\text{--}11.7 \text{ km s}^{-1}$). $V_\odot = 7.5 \text{ km s}^{-1}$ falls near the median of published values ($3\text{--}14 \text{ km s}^{-1}$, with a couple estimates near 20 km s^{-1}). Our $W_\odot = 4.5 \text{ km s}^{-1}$ is considerably smaller than the narrow range of $6.5\text{--}7.5 \text{ km s}^{-1}$ generally produced by other studies. Values larger than 5.0 km s^{-1} produce significantly poorer agreement with our stated boundary conditions. It may be the case that the OB central stars of SBN have a systematically smaller z component relative to other (older) stellar populations that inform other studies. We do not attempt to estimate uncertainties on $[U_\odot, V_\odot, W_\odot]$ owing to the small number of objects involved and the imprecise nature of the boundary conditions adopted. Uncertainties of $\pm 1.5 \text{ km s}^{-1}$ are plausible and used in Monte Carlo error propagation, where needed.

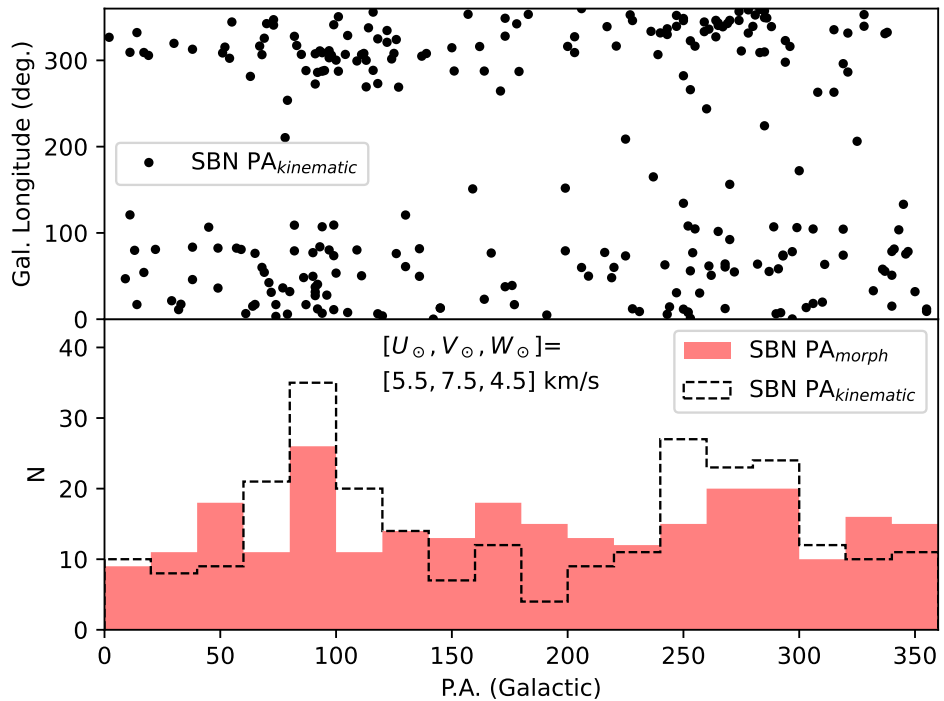


Figure 9. (upper panel) Galactic longitude versus kinematic position angle for the SBN central star sample. (lower panel) Distributions of SBN morphological position angles (red histogram) and central star kinematic position angles (dashed histogram). The two are consistent with having been drawn from the same parent population.

Table 1. Kinematic Data of 25 Runaway GOSC Stars

GOSC ID	Alias	<i>RUWE</i>	v_{2D}	σ_{v2D}	\overline{RV}_{\odot}	$\overline{\sigma_{RV}}$	RV RMS	$P(\chi^2, \nu)$	SpecType	Obs. Dates
					(km s $^{-1}$)	(km s $^{-1}$)				
(1)	(2)	(3)	(4)	(5)	(6)	(7)	(8)	(9)	(10)	(11)
20	ALS 11244	1.047	30	1	-39	18	7	0.981	O5If	628.96, 674.98, 712.97, 747.77, 786.55
27	ALS 12688	1.034	85	5	-184	30	104	0.000	O5.5V	668.97, 694.84, 747.79, 779.56, 786.56
78	BD+39 1328	1.298	38	4	-112	5	10	0.004	O8.5Iab	764.96, 724.97, 731.97
80	BD+43 3654	0.937	45	2	-53	10	6	0.798	O4If	628.96, 712.97, 747.78, 779.56, 786.56
82	BD+50 886	1.043	37	3	-36	9	9	0.524	O4V	668.96, 724.95, 731.91
88	BD+60 134	0.930	86	3	-100	11	19	0.027	O5.5V	712.98, 724.95, 725.92, 779.58, 786.57
90	BD+60 261	0.882	45	2	-77	4	4	0.405	O7.5III	712.99, 725.94, 779.59, 786.57
106	BD-10 4682	1.096	33	3	6	14	26	0.031	O7Vn	747.57, 752.57, 779.54
206	HD 12323	0.988	64	6	-47	3	30	0.000	ON9.2V	694.87, 712.99, 725.95, 786.57
207	HD 12993	0.950	25	3	-91	3	4	0.000	O6.5V	694.86, 713.00, 725.96, 786.58
221	HD 13745	0.953	49	4	-28	4	5	0.283	O9.7II	668.95, 724.91, 725.87, 786.58
234	HD 15137	0.936	44	4	-46	7	6	0.572	O9.5III	668.95, 724.93, 725.88, 786.58
238	HD 15642	0.837	32	2	-34	11	8	0.686	O9.5III	668.95, 724.94, 725.90, 786.58
282	HD 16691	0.917	42	2	-81	18	10	0.752	O4If	668.96, 724.94, 725.91
326	HD 18409	1.075	42	3	-60	3	7	0.054	O9.7Ib	668.96, 724.95, 725.91
340	HD 192281	0.972	33	1	-42	13	12	0.729	O4.5V	628.95, 674.97, 712.96, 747.58, 752.58, 779.57, 786.55
341	HD 192639	0.909	39	2	-17	4	6	0.041	O7.5Iabf	628.95, 674.97, 712.96, 747.58, 752.59, 779.57, 786.55
346	HD 193682	0.948	40	2	-40	6	10	0.019	O4.5IV	628.95, 674.98, 712.96, 747.77, 752.59, 779.57, 786.55
348	HD 195592	0.897	49	2	-104	7	15	0.002	O9.7Ia	628.96, 674.98, 712.97, 747.78, 779.55, 786.55
350	HD 201345	1.132	58	5	14	2	4	0.009	ON9.2IV	628.97, 674.99, 712.98, 747.78, 779.56
351	HD 202124	0.984	61	4	-55	4	7	0.003	O9Iab	628.97, 694.83, 712.98, 747.78, 779.56, 786.56
359	HD 210809	0.898	28	6	-89	3	12	0.000	O9Iab	628.97, 694.83, 712.98, 747.79, 779.56
365	HD 218915	0.966	52	6	-89	2	6	0.000	O9.2Iab	668.97, 694.85, 712.98, 747.79, 779.57, 786.57
403	HD 5689	0.961	53	3	-88	6	5	0.673	O7Vn	712.99, 725.93, 779.58, 786.57
474	HD 227018	1.073	42	2	4	2	4	0.038	O6.5V	674.97, 747.58, 752.58, 779.57, 786.54

NOTE—(1) GOSC source identification number, (2) common alias, (3) Gaia EDR3 re-normalized unit weight error, (4) projected two-dimensional peculiar velocity v_{2D} , (5) uncertainty on v_{2D} , (6) mean Heliocentric radial velocity, (7) mean radial velocity uncertainty, (8) radial velocity RMS, (9) probability of the null hypothesis; probabilities < 0.05 are considered multiple-star candidates, (10) literature spectral type and luminosity class, (11) Dates of observation for radial velocity data in Heliocentric Julian Date minus 2,458,000.

Table 2. Astrometric Data for Selected SBN Central Stars

SBN ID	Alias	α (2000) (deg.)	δ (2000) (deg.)	EDR3 ID (mag.)	G (mag.)	Env.	π (mas)	σ_π (mas yr $^{-1}$)	μ_α (mas yr $^{-1}$)	σ_{μ_α} (mas yr $^{-1}$)	μ_δ (mas yr $^{-1}$)	σ_{μ_δ} (mas yr $^{-1}$)	Code	Sp.T.	Ref.
(1)	(2)	(3)	(4)	(5)	(6)	(7)	(8)	(9)	(10)	(11)	(12)	(13)	(14)	(15)	(16)
1	...	267.0320	-29.1321	4057291747277127040	10.73	I	0.3510	0.0180	1.2820	0.0180	-1.2100	0.0110	3	(OB+)	S71
2	...	267.6164	-29.2128	4057244154701712900	15.75	I	0.4600	0.0650	-1.0050	0.0670	-2.3060	0.0410	3
3	...	267.1745	-28.1110	4057634103373474560	16.29	H	0.6370	0.0520	-2.2260	0.0610	-12.1090	0.0370	3	B	...
7	...	269.6277	-26.1637	4064254301560852332	12.74	FB	0.8220	0.0170	1.9260	0.0200	-1.8690	0.0140	3
10	HD 314937	270.0728	-25.2374	4064417063652618752	10.62	I	0.4060	0.0170	0.8920	0.0160	-2.1000	0.0120	3	(B)	N95
12	...	270.2554	-24.3596	4069013291115920256	13.52	I	0.2680	0.0200	-0.1330	0.0210	-2.5960	0.0150	3	OB	...
14	...	270.1691	-23.6141	4069123317001611648	16.75	H	0.3300	0.0790	-0.6790	0.0730	-1.9400	0.0510	3
16	...	270.2301	-22.9603	4069437463777653632	11.68	I	0.3260	0.0200	0.1280	0.0190	-0.9850	0.0140	3	B	...
17	...	270.8894	-22.5773	4069661459230981888	13.32	I	0.3010	0.0160	-0.3420	0.0200	-1.5410	0.0140	3	B	...
18	...	271.0645	-21.7705	4070010863401512320	13.60	I	0.2190	0.0310	-0.3390	0.0400	-1.5800	0.0250	3
19	...	271.2966	-21.0787	4070114011339898496	11.97	I	0.3130	0.0170	-1.8000	0.0160	-0.2760	0.0110	3	B	...
26	...	272.9675	-19.6154	4094704481502396288	11.70	H	0.3060	0.0140	0.3150	0.0160	-0.8520	0.0120	3	OB	...
27	...	273.0543	-19.5900	40946932158228561920	10.75	H	0.5550	0.0150	0.2380	0.0180	-1.6720	0.0120	3	(OB)	S71
28	...	272.3533	-18.6331	4095751942430811776	13.17	FH	0.2580	0.0170	-0.4440	0.0170	-2.6650	0.0130	3	B	...
29	...	272.2729	-18.2370	4095796884969650432	16.31	I	0.4160	0.0530	0.4130	0.0750	-1.0050	0.0550	3
32	...	273.5034	-18.4298	40956297592112338400	13.76	I	0.2660	0.0220	-0.6280	0.0230	-2.2440	0.0180	3	B+B	...
36	...	273.5010	-17.8755	4095733663064328960	15.81	I	0.2270	0.0540	0.3360	0.0640	-1.7980	0.0490	3
37	...	273.7007	-17.7360	4097225975217722112	14.43	I	0.3140	0.0250	0.3950	0.0250	-1.5300	0.0190	3	B	...
39	...	272.1834	-16.4332	4144151619667384704	11.49	I	0.2530	0.0240	-3.3640	0.0250	-3.2050	0.0190	3
45	...	274.2554	-16.5676	4097599225052642048	14.29	FB	0.2700	0.0370	-0.3340	0.0440	-2.9510	0.0340	3
51	...	275.0946	-16.1428	40980032911268883584	12.61	FH	0.7050	0.0230	0.3390	0.0220	-1.5990	0.0150	3	(O8V)	S17
54	HD 165319	271.4951	-14.1981	4147125180140397440	7.72	FH	0.6840	0.0280	-2.4050	0.0240	-1.2050	0.0180	1	O(O:0.71b)	S11
63	BD-13 4934	274.7732	-13.9140	4146594386587183360	9.35	FH	0.5690	0.0180	0.3750	0.0200	-1.7220	0.0160	3	(B1V)	H93
64	BD-14 5040	276.4121	-14.7516	4104201586232296960	10.02	I	0.5830	0.0150	5.8690	0.0180	-4.9170	0.0130	3	(O5.5V)	M16
65	BD-13 4937	274.8335	-13.9060	4146594906281063368	10.58	FH/FB	0.5510	0.0170	0.1480	0.0180	-1.5500	0.0140	3	(B1.5V)	W07
66	...	273.8499	-13.3266	4147436097099460224	10.82	I	0.5250	0.0200	-2.3700	0.0200	-0.1300	0.0160	3
67	NGC6611-ESL45	274.5685	-13.6078	4146617819936287488	11.52	H/FB	0.5370	0.0190	0.1860	0.0200	-1.4780	0.0160	3	(O9V)	H93
83	...	276.7053	-11.6111	4153376178622946560	14.34	I	0.3470	0.0250	-0.9390	0.0290	-2.2430	0.0230	2	Be	...
89	...	278.0976	-10.5369	4154922110668953728	14.21	FH	0.3860	0.0240	-0.5770	0.0240	-1.8100	0.0190	3	B	...
101	...	277.8861	-8.4803	4156594925877520512	12.06	H/FB	0.4410	0.0230	0.2440	0.0240	-2.2880	0.0200	3	B	...
129	TYC 5121-625-1	280.1412	-4.8898	4256661923166288640	10.07	FB	0.8910	0.0340	1.5920	0.0410	-0.9240	0.0320	3
157	...	282.3236	-1.2910	4260025061295449344	17.09	FB	0.4600	0.0890	1.7750	0.0910	1.2990	0.0790	3
163	...	282.1649	-0.7789	4266110686393370112	13.14	I	0.2050	0.0150	-2.0820	0.0170	-4.3790	0.0140	3	B	...
165	...	282.8876	-1.0416	4265524787208443392	14.80	I	0.2500	0.0360	-0.8620	0.0330	-2.2670	0.0320	3
173	...	283.3701	-0.2024	4266203560776207360	16.06	I	0.2350	0.0540	-2.5490	0.0590	-4.0610	0.0520	3

KOBULNICKY & CHICK

Table 2 *continued on next page*

Table 2 (*continued*)

SBN ID	Alias	α (2000)	δ (2000)	EDR3 ID	G	Env.	π	σ_π	μ_α	σ_{μ_α}	μ_δ	σ_{μ_δ}	Code	Sp.T.	Ref.
(1)	(2)	(3)	(4)	(5)	(6)	(7)	(8)	(9)	(10)	(11)	(12)	(13)	(14)	(15)	(16)
195	...	284.5546	+2.6318	4268636325380123776	15.74	I	0.2160	0.0490	-1.9660	0.0670	-4.2830	0.0510	3
197	...	283.7461	+3.3152	4280988281262754816	14.87	FB	0.2440	0.0520	-1.4550	0.0660	-3.3370	0.0500	3
200	...	285.5369	+3.5131	4268848088051429888	12.70	I	0.2210	0.0220	-1.0280	0.0210	-3.0060	0.0200	2	B	...
203	...	284.7421	+4.3312	4281521029003333888	14.86	I	0.4460	0.0500	-0.3900	0.0490	-4.1270	0.0480	3
212	...	286.2944	+5.1635	4281497595674391040	12.12	I	0.3840	0.0190	-0.4160	0.0210	-4.2110	0.0160	1	B	...
240	HD 230561	285.9196	+13.0533	4314239746302505216	10.57	I	0.7870	0.0140	-1.4310	0.0150	-2.5020	0.0150	2	B	...
249	...	288.7825	+12.7018	4313233624439996416	14.19	I	0.1440	0.0230	-3.3320	0.0170	-5.7790	0.0160	2	Be	...
252	...	290.0852	+13.3686	431919284006688384	14.49	I	0.2020	0.0260	-2.2800	0.0220	-5.8890	0.0200	3	B	...
255	TYC 1054-952-1	289.7334	+13.7164	4319404186763499264	10.98	FH	0.7860	0.0150	0.6700	0.0120	-1.3950	0.0120	2	B	...
263	...	291.3945	+14.5000	4319746920840845824	14.59	I	0.1970	0.0300	-0.8930	0.0280	-5.1720	0.0240	3	O	...
265	...	290.5179	+14.9759	4319932433377440384	13.25	I	0.2130	0.0150	-2.0550	0.0130	-4.8220	0.0120	2	B	...
268	...	290.4429	+15.2522	4320784289011907840	14.69	FH	1.1650	0.0200	0.7670	0.0190	-6.9890	0.0170	3
271	...	290.9593	+15.4775	4320067604583046144	14.20	I	0.2400	0.0220	-1.7780	0.0190	-4.8310	0.0200	2	OB	...
272	...	288.4517	+17.4043	4513609516844356352	11.71	I	0.1060	0.0140	-4.2900	0.0120	-5.6180	0.0130	1	B	...
282	...	292.4360	+18.1956	4323221175735917952	12.97	FH	0.1800	0.0190	-1.7570	0.0200	-4.5340	0.0190	2	B	...
284	...	292.2422	+19.1435	4323443105304174336	14.31	FH	0.1140	0.0210	-3.5180	0.0200	-5.0300	0.0200	2	OB	...
285	...	292.1115	+19.3995	4515605611463119104	14.96	FH	0.2460	0.0250	-2.1550	0.0230	-3.5080	0.0240	1	OB	...
287	...	292.4086	+19.7662	2017632909648231680	16.82	I	0.2780	0.0680	-2.6250	0.0720	-5.8530	0.0750	3
288	HD 350123	293.1847	+19.9780	1825504041654597760	10.87	I	0.3430	0.0130	-2.7360	0.0120	-5.6990	0.0140	2	B	...
289	...	293.0017	+20.3677	201777288688396392	12.32	I	0.4300	0.0210	-3.2030	0.0180	-4.5970	0.0220	3	M	...
291	...	294.0481	+20.3533	1825621826822510848	15.51	FH	0.1500	0.0320	-3.0030	0.0310	-6.1270	0.0290	3	B	...
295	...	294.3432	+22.3971	2018445929744491904	15.62	I	0.2250	0.0310	-2.9450	0.0270	-5.5110	0.0300	3
296	...	295.1029	+22.5099	201993776086774208	15.10	I	0.1510	0.0330	-3.1040	0.0230	-5.8500	0.0300	3
298	HD 345117	297.7841	+22.8318	1827989092255873440	8.98	I	0.3700	0.0160	-1.3180	0.0090	-6.4980	0.0160	2	B(B3)	N95
300	HD 344765	296.0836	+23.8792	202014400336761984	10.52	I	0.4870	0.0110	-1.9360	0.0070	-5.1440	0.0100	2	B(B8)	N95
303	...	296.5557	+24.1172	2020550906090165504	12.69	I	0.0870	0.0190	-2.9890	0.0130	-5.5300	0.0160	1	Be	...
306	BD+243883	296.8391	+24.5622	2020657666110700544	10.01	I	0.4590	0.0130	-1.7450	0.0090	-5.0150	0.0130	2	B(OB)	S60
309	...	296.0031	+25.8131	2021727319135074048	13.22	H	0.1150	0.0280	-2.9110	0.0210	-5.6170	0.0280	3	M	...
313	...	299.3242	+26.1805	2027201512642636480	16.18	H	0.2950	0.0370	-3.2890	0.0280	-5.4870	0.0340	3
314	HD 338961	297.6017	+27.4655	2028000853284283904	10.90	I	0.2210	0.0150	-3.2140	0.0110	-6.0040	0.0130	3	B+B	...
315	...	296.6638	+28.2231	2028281679782393728	14.31	I	0.0970	0.0170	-2.9190	0.0150	-5.4460	0.0180	3	M	...
318	...	305.7449	+34.2393	2056257413069916160	16.34	H	1.4650	0.0490	-3.6690	0.0470	-6.9680	0.0490	3
319	...	301.4088	+36.6606	2059899472309137664	12.17	I	0.0950	0.0100	-2.3270	0.0100	-4.2090	0.0110	1	Be	...
320	HD 191611	302.3886	+36.4888	2059236196250413696	8.48	I	0.3150	0.0160	-2.5780	0.0160	-5.1390	0.0190	2	OB	...
321	...	303.6587	+36.4972	206043282942111488	13.20	H	0.2110	0.0110	-3.2040	0.0110	-5.1710	0.0130	2	OB	...
322	...	303.7729	+36.5995	2060507437839909248	12.58	H	0.2030	0.0100	-3.0930	0.0100	-5.1500	0.0110	1	O	...
324	TYC 3151-2909-1	303.3705	+38.2421	2060924324545985152	10.92	I	0.1880	0.0110	-4.2700	0.0110	-4.5890	0.0120	2	OB	...

KINEMATICS OF BOWSHOCK STARS

Table 2 *continued on next page*

Table 2 (continued)

SBN ID	Alias	α (2000) (deg.)	δ (2000) (deg.)	EDR3 ID	G (mag.)	Env.	π (mas)	σ_π (mas)	μ_α (mas yr $^{-1}$)	σ_{μ_α} (mas yr $^{-1}$)	μ_δ (mas yr $^{-1}$)	σ_{μ_δ} (mas yr $^{-1}$)	Code	Sp.T.	Ref.
(1)	(2)	(3)	(4)	(5)	(6)	(7)	(8)	(9)	(10)	(11)	(12)	(13)	(14)	(15)	(16)
326	TYC 2697-1046-1	308.2344	+36.2001	2056918391351771904	10.64	H	0.3000	0.0120	-2.2800	0.0110	-4.7850	0.0130	2	B(B1V)	K10
328	...	308.8935	+36.5737	2062750888226081024	11.90	H	0.3070	0.0110	-2.1890	0.0090	-5.2910	0.0100	2	OB	...
329	...	307.3419	+37.9290	2063868163830050176	14.08	I	0.4120	0.0190	-4.0020	0.0180	-8.3250	0.0210	2	O	...
330	HD 229159	305.7251	+39.2980	2061232084708040320	8.19	H	0.5850	0.0180	-2.0140	0.0170	-5.8030	0.0200	2	B(B1.5Ib)	H56
331	LSII +39 53	306.8232	+39.7424	2067267304028045568	9.90	H/FB	0.5920	0.0140	-3.3140	0.0140	-5.3880	0.0150	1	O(O8V)	S11
332	...	306.6037	+40.0281	2067287576272381568	11.67	FB	0.5770	0.0140	-3.1000	0.0140	-4.4590	0.0160	1	OB(O9.2III)	B18
333	...	306.6949	+40.0991	2067382031192434816	12.99	H	0.5580	0.0340	-2.9290	0.0330	-4.7140	0.0390	3	OB+OB	...
335	TYC3156-1106-1	307.0641	+40.7436	206742405315279558	10.61	H	0.4970	0.0120	-1.9570	0.0120	-4.1850	0.0130	2	B	...
336	...	309.1355	+39.6131	2064436860058004096	14.34	H	0.5840	0.0290	-0.7270	0.0300	-7.2410	0.0360	3	OB	...
338	CPR2002 A10	308.7296	+40.5790	2064738049323468928	13.79	I	0.5830	0.0250	-2.6390	0.0240	-4.4710	0.0310	2	O(O9V)	K10
339	CPR2002 A37	309.0188	+40.9370	2064838375463800448	11.64	FH	0.6320	0.0180	4.7260	0.0180	2.3220	0.0190	2	O(O5V)	B18
340	HD 19522	307.1260	+42.0098	2068107876366768768	7.62	FH	0.6790	0.0210	-0.4610	0.0220	-3.4690	0.0250	2	B(B0.2III)	W71
341	...	308.6206	+41.9380	2067963015711183744	12.04	I	0.5650	0.0150	-2.2190	0.0170	-3.8840	0.0170	1	OB(O9V)	B18
342	...	308.6439	+41.9749	2067963535403817728	14.51	I	0.6560	0.0170	-3.0980	0.0180	-2.9160	0.0190	2	OB(B1V)	K10
343	HD 195592	307.6457	+44.3152	2070636448174993024	6.71	I	0.5600	0.0170	-2.5060	0.0170	1.0610	0.0170	2	OB(O9.7Ia)	S11
344	BD+43 3654	308.4003	+43.9854	2069819545390584192	9.13	I	0.5820	0.0120	-2.5950	0.0140	0.7290	0.0140	3	(O4I)	M16
345	HD 199201	313.2217	+42.6077	2065970601862601728	8.25	I	1.2440	0.0150	-1.0600	0.0180	-3.6570	0.0170	2	OB(B1V)	K10
346	NSVS 575390	312.9592	+43.3249	206674304885540992	12.53	FH	0.2720	0.0150	-2.7390	0.0150	-4.0500	0.0170	1	OB(O9.7Ia)	S11
349	TYC 3597-970-1	320.4128	+50.0336	2171121468681724672	11.00	I	0.2350	0.0110	-4.0100	0.0130	-4.5590	0.0130	2	B(OB)	H64
351	TYC 3973-198-1	333.1253	+55.5354	2006096696161332996	11.27	I	1.0470	0.0170	2.6420	0.0210	-2.1750	0.0180	2	OB	...
352	...	333.9895	+58.1601	219879985284078352	13.49	I	0.1730	0.0120	-2.8650	0.0130	-1.9620	0.0120	2	B	...
353	...	334.1372	+59.3919	2201205412482296448	11.59	I	0.2150	0.0110	-6.1560	0.0120	-1.3010	0.0120	2	O	...
354	KW97 63-24	336.9226	+57.6846	200776255752593664	11.82	I	0.1260	0.0120	-2.4630	0.0130	-1.8850	0.0110	3	Be	...
356	HD 240015	339.8238	+59.0168	2008430237808841600	9.84	H	0.3580	0.0120	-2.7470	0.0130	-1.9110	0.0130	1	B(B2)	C93
358	TYC 4264-1036-1	338.5271	+60.9806	2201736029920376960	10.23	I	1.1520	0.0120	-2.3410	0.0120	-2.8120	0.0140	2	B(B)	H64
359	HD 215806	341.6676	+58.2855	20074405058871856768	9.07	FH	0.3790	0.0140	-2.4910	0.0150	-2.2310	0.0130	2	O(B0Ib)	H56
360	HD 216411	342.8907	+59.0085	2014236243312284800	7.00	I	0.3300	0.0150	-6.8680	0.0170	-6.0980	0.0160	1	B	...
361	TYC 4278-522-1	342.9155	+61.1475	2206818556775783552	10.09	I	1.2190	0.0130	-1.8530	0.0130	-1.1080	0.0130	1	B	...
362	...	343.9389	+60.4112	2014562519088745344	12.64	I	1.2570	0.0110	-1.7390	0.0130	-1.5230	0.0120	2	B	...
365	HD 2619	7.6180	+65.2721	527356876544834688	8.14	I	1.9450	0.0170	-0.5970	0.0160	-2.2350	0.0160	2	B(B0.5III)	H56
366	HD 2083	6.4635	+71.8071	53710693343756800	6.87	I	0.9810	0.0280	-0.4740	0.0300	0.9830	0.0300	3	B(B2)	...
367	LSI+60 226	34.4717	+61.1869	50768681968507208	10.46	I	0.4760	0.0130	-0.8130	0.0120	-0.2570	0.0160	2	B(OB)	H64
368	KM Cas	37.3769	+61.4956	465523778576137600	10.83	FB/FH	0.5050	0.0160	-1.4080	0.0130	-0.7040	0.0150	3	O(O9.5V)	M95
371	TYC 3339-851-1	61.4710	+51.1161	25068408558334848	11.28	I	1.3340	0.0210	-0.3750	0.0230	-1.9380	0.0190	1	O(O5V)	R19
372	...	62.7947	+50.7082	271629679020572544	10.91	I	1.3320	0.0180	-0.9540	0.0190	-1.1760	0.0140	1	OB	...
373	HD 21856	53.1667	+35.4617	2219807160662833.36	5.87	I	2.4060	0.0870	-8.8860	0.1010	1.6670	0.0780	3	B(B3)	C93
374	HD 41161	91.4685	+48.2493	96982376583544576	6.72	I	0.6710	0.0610	-2.5160	0.0600	-1.2890	0.0480	3	(O8V)	S11

Table 2 continued on next page

Table 2 (*continued*)

SBN ID	Alias	α (2000) (deg.)	δ (2000) (deg.)	EDR3 ID	G (mag.)	Env.	π (mas)	σ_π (mas yr $^{-1}$)	μ_α (mas yr $^{-1}$)	σ_{μ_α} (mas yr $^{-1}$)	μ_δ (mas yr $^{-1}$)	σ_{μ_δ} (mas yr $^{-1}$)	Code	Sp.T.	Ref.
(1)	(2)	(3)	(4)	(5)	(6)	(7)	(8)	(9)	(10)	(11)	(12)	(13)	(14)	(15)	(16)
375	Ae Aur	79.0756	+34.3125	182071570715713024	5.94	FB	2.5740	0.0340	-4.7470	0.0460	43.5380	0.0330	3	(O9.5V)	S11
376	HD 48099	100.4968	+6.3454	3132668164099141120	6.31	I	0.7630	0.0420	1.0430	0.0440	2.7520	0.0390	3	(O5V+O9V)	S11
377	HD 46573	98.5982	+2.5342	3130004665899281024	7.83	I	0.7280	0.0230	-7.2080	0.0250	1.0320	0.0220	3	(O7V)	S11
378	Ups Ori	82.9827	-7.3016	3016424530632449280	4.55	I	2.4570	0.1400	-0.7040	0.1200	-4.8850	0.1040	3	(O9.7V)	S11
381	HD 54662	107.3344	-10.3466	3046582725837564800	6.17	I	0.7240	0.0530	-2.5370	0.0410	3.1280	0.0470	3	(O6V+O7V)	S11
383	CD-26 5136	118.2542	-27.1160	5601917842664443520	9.54	I	0.1590	0.0140	-3.6900	0.0100	4.5210	0.0120	3	(O6.5Iab)	S14
384	CD-35 4415	124.1337	-35.6480	5543183649492723584	10.34	FB	0.2920	0.0120	-2.8110	0.0110	3.4650	0.0130	3	(O7III)	V93
385	CD-41 4637	133.8653	-41.5895	5524471473410215808	9.52	I	0.4250	0.0130	-4.9080	0.0130	6.9240	0.0130	3	(O6Ib)	V93
386	Vel X-1	135.5586	-40.5547	5620057678322625920	6.74	I	0.4960	0.0150	-4.8220	0.0150	9.2820	0.0160	3	(B0.5Ia)	H78
389	HD 76031	133.0172	-44.0097	5331660839484919936	8.85	FH	0.5520	0.0250	-6.1370	0.0280	4.0270	0.0270	3	(B1Iab)	H78
390	CD-44 4967	134.1186	-45.3588	53312981337876769536	10.01	I	0.5860	0.0100	-6.9430	0.0120	5.8050	0.0130	3	(OB)	H78
391	HD 77207	134.821	-48.8303	53254524841440825600	9.19	FH	0.5530	0.0170	-5.3590	0.0180	3.6770	0.0170	3	(B7Iab)	H78
393	CD-48 4287	134.5433	-49.3965	53252494770245772544	9.96	FH	0.5220	0.0120	-5.1290	0.0150	3.8140	0.0150	3	(OB)	M54
394	HD 29831.0	138.8260	-51.3867	5313479796251809664	9.78	I	0.5130	0.0110	-1.1090	0.0120	-0.4170	0.0130	3	(B0)	R03
395	HD 29835.3	139.1552	-51.9396	5311906841793959936	9.85	I	0.3650	0.0120	-5.0880	0.0150	3.6510	0.0150	3	(O)	R03
396	...	150.7137	-56.9004	52597125751381110208	15.33	FH	0.2430	0.0250	-3.9340	0.0290	3.4070	0.0300	3
397	CD-55 3196	153.0851	-56.3427	5259053730157539328	10.47	I	0.3660	0.0130	-8.1750	0.0150	4.1070	0.0140	3	(O9.5III)	P12
404	CD-59 3123	157.5869	-59.8226	5255179905867530752	9.71	FH	0.2740	0.0120	-5.2450	0.0130	2.4620	0.0120	3	(O9.5Ib)	V93
405	HD 303197	159.5797	-58.8633	5350640192585837568	9.14	FH	0.4190	0.0130	-7.1200	0.0150	3.4590	0.0130	3	(B3III)	N95
406	HD 92607	160.0517	-59.8028	52544785392580508288	8.11	FH	0.3430	0.0270	-6.8920	0.0310	2.4930	0.0290	3	(O9IV)	S14
407	HD 93249	161.1828	-59.3570	5350395383778733568	8.30	FH	0.3970	0.0180	-6.0050	0.0190	2.0420	0.0180	3	(O9III)	S14
408	CPD-58 2625	161.0038	-59.5960	53503626338946360960	10.50	FH	0.3850	0.0190	-6.3690	0.0210	2.5570	0.0210	3	(O9.2V)	S14
409	HD 93027	160.8247	-60.1342	5254268518156437888	8.69	FH	0.3420	0.0240	-7.1170	0.0300	1.9410	0.0260	3	(O9.5IV)	S14
410	HD 305536	161.0461	-60.0560	5254289961265754368	8.91	H	0.4260	0.0210	-7.0380	0.0230	1.8410	0.0210	3	(O9.5+B)	S14
411	HD 305599	162.3541	-59.8288	5338310887667141888	9.90	FH	0.4530	0.0120	-6.1130	0.0140	2.2510	0.0120	3	(B0V)	A16
412	...	161.9426	-60.4100	5350276636517384064	15.71	FH	0.4310	0.0370	-6.4500	0.0420	2.4080	0.0400	3
414	HD 93858	162.1938	-60.5944	5242184954087251456	9.00	FH	0.4260	0.0150	-6.8520	0.0170	2.4740	0.0160	3	(B0.5III+?)	A16
422	...	184.8500	-62.9367	605422734264543200	12.14	FH	0.2770	0.0110	-6.3290	0.0110	0.0800	0.0130	3
425	...	186.6434	-62.8721	6054565044886660608	13.06	FH	0.2540	0.0120	-6.0220	0.0110	-0.3420	0.0140	3
426	ALS 19363	186.9957	-62.7333	6054571524119925248	12.07	FH	0.3000	0.0110	-5.8360	0.0100	-0.3490	0.0120	3
430	...	190.1224	-62.0485	60554517175188558240	14.14	I	0.2460	0.0180	-6.6360	0.0160	-0.4360	0.0210	3
431	DY Cru	191.8528	-59.6947	6056720389175393024	6.97	I	0.8430	0.0220	-5.4330	0.0190	0.7400	0.0220	3	(C-N5.5)	B96
434	...	192.9744	-62.2905	605524597139954968	11.94	I	0.2700	0.0120	-2.1280	0.0100	-1.1280	0.0120	3
440	...	197.0812	-62.8286	5862415374487312896	11.85	I	0.1070	0.0190	-6.5260	0.0150	-0.7140	0.0210	3
445	...	199.4634	-62.8228	5862274774485353344	15.38	I	0.1670	0.0280	-6.7680	0.0220	-1.0300	0.0270	3
448	...	200.9227	-62.8703	586823144741454144	12.69	I	0.1820	0.0130	-6.3970	0.0100	-0.9990	0.0130	3
449	...	200.8843	-62.11750	586832188224088736	13.87	I	0.2020	0.0150	-6.2160	0.0130	-1.3600	0.0160	3

Table 2 *continued on next page*

Table 2 (*continued*)

SBN ID	Alias	α (2000)	δ (2000)	EDR3 ID	G	Env.	π	σ_π	μ_α	σ_{μ_α}	μ_δ	σ_{μ_δ}	Code	Sp.T.	Ref.
(1)	(2)	(3)	(4)	(5)	(6)	(7)	(8)	(9)	(10)	(11)	(12)	(13)	(14)	(15)	(16)
450	...	201.0913	-62.8361	586820588420671104	14.59	I	0.1540	0.0230	-6.9930	0.0200	-1.2170	0.0230	3
453	...	201.3016	-61.9602	586831021931539584	14.08	I	0.2630	0.0180	-5.7180	0.0140	-1.4780	0.0190	3
458	...	203.1408	-62.6347	5865293483625515904	13.67	FH	0.1680	0.0160	-6.1470	0.0120	-1.3200	0.0150	3
462	...	203.7579	-62.4014	5865351375446364288	12.26	I	0.2430	0.0110	-6.0900	0.0080	-2.0050	0.0110	3
463	TYC 8995-1548-1	203.8614	-62.1872	5865357598905884288	11.58	I	0.2750	0.0160	-6.2380	0.0110	-1.7010	0.0160	3
464	...	203.9370	-62.2169	5865731806467529984	11.28	I	0.2640	0.0180	-6.0120	0.0140	-1.8130	0.0180	3
467	...	204.7837	-61.4636	5865788229491570176	12.78	I	0.2310	0.0120	-6.2250	0.0090	-1.2240	0.0110	3
468	...	205.6564	-62.1080	5865701058828885120	15.65	I	0.1680	0.0360	-6.1860	0.0260	-1.5950	0.0300	3
469	...	205.9714	-62.0164	5865515854573028352	13.80	H	0.2470	0.0160	-6.5040	0.0110	-1.8050	0.0130	3
470	...	206.0151	-62.1109	586551122126799336	14.60	H	0.2240	0.0240	-6.5990	0.0160	-1.9590	0.0190	3
471	...	206.1022	-61.9824	5865609764995791616	14.02	FH	0.2910	0.0200	-6.3640	0.0140	-1.7600	0.0160	3
473	...	207.0750	-63.1576	5864600958756320128	11.93	I	0.2950	0.0130	-6.2330	0.0090	-1.5710	0.0110	3
474	...	207.9211	-62.7460	5864706821111715456	12.33	I	0.3120	0.0110	-6.7560	0.0070	-1.9810	0.0090	3
484	...	209.9278	-61.8872	5866279779893013376	17.01	I	0.3680	0.0660	-7.1980	0.0410	-2.4810	0.0510	3
485	...	209.8673	-61.3831	5866357016275122688	12.02	H	0.3020	0.0180	-5.0750	0.0110	-1.9170	0.0140	3
489	...	210.4406	-61.6376	5866285732847818496	13.44	I	0.2620	0.0250	-3.4700	0.0160	-1.7620	0.0200	3
497	...	213.7207	-60.9954	5866610148776042496	17.06	H	0.6160	0.0660	-5.4430	0.0600	-1.3560	0.0940	3
506	HD 126593	217.2119	-60.5403	5878638565442923648	8.51	I	0.3930	0.0230	-5.2680	0.0210	-2.9070	0.0230	3	(B11b)	H75
509	...	218.2106	-59.7056	5878825379365317760	12.73	I	0.2190	0.0340	-4.9870	0.0280	-1.5280	0.0330	3
512	...	220.2217	-60.4021	5878514831732241408	13.07	I	0.2270	0.0390	-5.0550	0.0340	-3.5770	0.0390	3
513	...	220.7322	-60.7329	5877741119142644864	12.32	I	0.3100	0.0140	-5.1710	0.0120	-2.9880	0.0130	3
514	...	220.6714	-60.6012	5877754901760339840	13.94	I	0.2800	0.0170	-5.2440	0.0150	-3.7120	0.0160	3
515	TYC 8692-53-1	220.7504	-59.9393	58778903169802137088	10.86	I	3.6650	0.0170	-29.5580	0.0140	-26.8960	0.0150	3
517	...	221.1265	-60.1617	587814612169605936	14.23	I	0.2540	0.0190	-5.5120	0.0170	-3.5120	0.0180	3
518	...	221.5572	-60.5366	5878076062193284480	14.67	I	0.2930	0.0220	-4.9160	0.0200	-2.9070	0.0200	3
520	...	222.2495	-59.7503	5878261295529449984	12.26	I	0.1890	0.0270	-4.6800	0.0210	-2.5020	0.0210	3
534	...	227.0427	-59.0702	5876631956753314816	13.43	I	0.3730	0.0540	-4.1930	0.0520	-2.7330	0.0600	3
539	...	229.2729	-58.6086	5877065061259329024	13.93	FH	0.1350	0.0180	-4.8780	0.0180	-0.0440	0.0220	3
544	HD 136003	230.1783	-56.1327	5886362600284099456	6.73	I	0.9380	0.0250	-7.7310	0.0220	-9.2130	0.0270	3	(B11ab)	H75
545	...	232.0861	-57.2918	5883074820003926528	15.05	I	0.2330	0.0540	-4.4000	0.0530	-3.4720	0.0540	3
548	...	236.2329	-55.7363	5884297751823946880	12.55	I	0.1730	0.0200	-4.3110	0.0210	-3.5280	0.0200	3
555	ALS 18049	236.0841	-53.9115	5885668499206748160	12.23	FB	0.4280	0.0130	-3.8520	0.0140	-2.1870	0.0140	3	(O9V)	M16
558	...	238.2823	-54.4797	5884651966378230528	12.75	FH	0.2240	0.0260	-3.3460	0.0290	-3.8590	0.0250	3
561	...	237.8154	-53.3798	5885047275139494656	16.93	I	0.4580	0.0690	-0.8880	0.0700	-1.5160	0.0680	3
575	HD 150898	251.8319	-58.3415	5927377029712024576	5.53	I	0.8810	0.0710	-5.5790	0.0650	-20.9610	0.0600	3	(B0Lab)	H75
579	CPD-51 8958	242.0179	-51.6085	5981519284362057728	11.34	I	0.4270	0.0230	-3.0240	0.0270	-2.8740	0.0200	3	(OB)	S71
581	HD 330345	241.0020	-49.8726	5983343889544384384	10.05	I	0.5420	0.0150	-3.1960	0.0160	-3.0690	0.0140	3	(B)	N95

Table 2 *continued on next page*

Table 2 (*continued*)

SBN ID	Alias	α (2000)	δ (2000)	EDR3 ID	G	Env.	π	σ_π	μ_α	σ_{μ_α}	μ_δ	σ_{μ_δ}	Code	Sp.T.	Ref.
(1)	(2)	(3)	(4)	(5)	(6)	(7)	(8)	(9)	(10)	(11)	(12)	(13)	(14)	(15)	(16)
583	...	242.9572	-51.2070	5934985856344703744	14.24	I	0.5380	0.0200	-3.5010	0.0240	-4.4270	0.0170	3	OB(OB)	S71
584	...	243.4445	-51.3071	5934954485901800576	15.96	FB/H	0.3700	0.0370	-2.4000	0.0460	-3.8970	0.0360	3
587	...	244.2157	-51.2413	5934852300064549504	14.24	FH	0.1890	0.0240	-3.2840	0.0260	-3.6170	0.0200	3
589	CD-49 10393	243.1612	-50.1335	5935169268617561344	11.07	FB	0.4390	0.0190	-2.6620	0.0200	-2.5310	0.0160	3
607	...	247.6430	-47.8189	5941947792177035776	14.83	FB	0.2430	0.0350	-2.4280	0.0360	-3.4260	0.0240	3
614	...	248.8306	-46.5083	59428673575166443456	12.27	I	0.2280	0.0170	-1.7740	0.0190	-2.6090	0.0130	3
616	...	250.4718	-45.9178	5943151168959618688	15.53	I	0.2770	0.0430	-2.8620	0.0530	-4.2450	0.0450	3
618	...	250.8866	-45.9529	5943095476117383296	16.63	I	0.5400	0.0700	-0.8390	0.0910	-3.8080	0.0670	3
619	...	250.4264	-45.2510	5943194324788194176	14.89	I	0.2260	0.0290	-3.1900	0.0340	-3.7850	0.0270	3
624	...	252.3550	-44.9800	596424231754517504	13.39	FH	0.2570	0.0160	-1.9700	0.0200	-3.2550	0.0160	3
626	...	253.4814	-45.1489	5964030074446095744	11.34	I	0.3930	0.0250	-0.7380	0.0300	-1.3380	0.0240	3
634	HD 152756	254.3125	-43.7209	5964575672745370752	8.83	FB	0.6240	0.0170	-0.4400	0.0210	-2.8850	0.0170	3	OB(B)	C93
635	...	253.8732	-43.1510	5964883879575434240	13.47	FH	0.3080	0.0260	-0.6790	0.0350	-1.1470	0.0280	3	O	...
636	...	253.7381	-42.9332	5964903842583554304	13.49	FH	0.3110	0.0170	-1.4280	0.0220	-2.7760	0.0180	3
641	...	254.6142	-42.77191	59662205421159336768	14.40	FH	0.2990	0.0480	-1.6320	0.0600	-2.9640	0.0470	3
648	...	256.2160	-42.1150	5965562308305643008	14.28	I	0.2450	0.0470	-2.0950	0.0660	-4.1340	0.0500	3	OB	...
653	...	257.1952	-40.5743	5966132787371809336	13.76	I	0.5620	0.0170	-0.4230	0.0210	-3.2480	0.0150	3	K	...
655	...	257.0100	-40.2734	5966890930670155520	13.73	I	0.3200	0.0180	-1.3390	0.0230	-2.7750	0.0150	3	B	...
656	...	258.0313	-40.7731	5972061491504971904	13.21	I	0.2940	0.0160	-1.6280	0.0200	-3.1780	0.0140	3
657	...	257.1885	-40.2836	59668933237076295040	15.43	I	0.2710	0.0390	-1.1940	0.0530	-2.6380	0.0380	3
662	HD 153426	255.3042	-38.2033	5970357660807157632	7.40	I	0.5850	0.0240	0.5240	0.0290	0.0910	0.0200	3	(O8.5III)	S14
667	HD 155775	258.8430	-38.2130	5973477318881351168	6.66	I	0.9970	0.0360	3.9680	0.0430	-6.5040	0.0310	3	(O9.7III)	S14
670	...	259.3004	-38.0560	59735616767380929056	14.75	I	0.5590	0.0260	-2.8080	0.0320	-4.2860	0.0210	3
673	...	260.1593	-38.0302	597219177374952192	13.52	FB	0.2580	0.0200	-1.0350	0.0230	-2.1110	0.0170	3	B	...
681	...	259.2521	-36.2267	5973948730168050560	13.06	FH	0.5310	0.0250	-0.2300	0.0280	-2.1200	0.0190	3
687	...	262.2491	-36.1152	5974877851854232192	13.19	I	0.3710	0.0210	-0.3390	0.0220	-2.4410	0.0160	3
691	...	260.7084	-34.0562	597610655609797824	12.79	I	0.5550	0.0210	-1.7440	0.0250	-1.6830	0.0160	3	(B0V)	G11
692	...	261.7568	-34.2231	5975945894262363776	10.79	H	0.5570	0.0190	1.4950	0.0210	-2.6660	0.0140	3	O(O7.5V)	G11
700	...	263.4495	-31.2742	4055247370601329024	13.16	I	0.2580	0.0210	-0.3890	0.0230	-1.5580	0.0150	3	OB	...
701	...	264.0186	-30.8320	4055427795853598464	13.43	FB	0.2960	0.0190	-0.5180	0.0230	-1.5150	0.0160	3
705	CD-29 13925	266.2842	-29.9459	4056844217038364928	10.24	FH	0.4260	0.0180	-1.1230	0.0210	-2.6040	0.0130	3	(B0.5Ib)	H56
709	...	266.8751	-29.2401	405727728502494080	11.44	FB/H	0.3750	0.0210	0.7610	0.0230	-2.2810	0.0140	3	OB+B	...
712	...	268.5652	-26.2899	4063921012088804608	12.96	I	0.2730	0.0270	0.4100	0.0310	0.2560	0.0180	3
713	...	270.7833	-24.3886	4066015925358007168	13.26	FB/H	0.8170	0.0260	0.6750	0.0220	-1.6850	0.0170	3
714	...	270.6218	-23.8261	4069147849854796288	11.18	H	0.3700	0.0300	0.3330	0.0380	-1.1930	0.0260	3
715	...	270.6745	-23.6339	40691163586614618240	11.98	H	0.5040	0.0240	0.2410	0.0290	-0.2540	0.0190	3
717	...	270.7511	-22.2186	4069876379388868864	12.92	H	0.3520	0.0210	0.3530	0.0240	-1.0960	0.0170	3

Table 2 *continued on next page*

Table 2 (*continued*)

SBN ID	Alias	α (2000) (deg.)	δ (2000) (deg.)	EDR3 ID	G (mag.)	Env.	π (mas)	σ_π (mas)	μ_α (mas yr $^{-1}$)	σ_{μ_α} (mas yr $^{-1}$)	μ_δ (mas yr $^{-1}$)	σ_{μ_δ} (mas yr $^{-1}$)	Code	Sp.T.	Ref.
(1)	(2)	(3)	(4)	(5)	(6)	(7)	(8)	(9)	(10)	(11)	(12)	(13)	(14)	(15)	(16)
718	...	271.3734	-22.5017	4069675924682487296	13.19	FB	0.2620	0.0170	-0.4650	0.0170	-2.7510	0.0130	3
720	...	272.1170	-21.6528	4069838308800203776	13.34	I	0.2450	0.0210	-0.2010	0.0200	-1.8540	0.0140	3
722	HD 166965	273.4641	-18.9895	4094753787724436480	8.63	FH	0.5490	0.0200	0.2470	0.0200	-1.5910	0.0160	3	(B2Ib)	H88
723	...	273.1051	-18.5457	4095578077849408384	12.90	FH	0.1620	0.0350	-0.8670	0.0370	-3.3230	0.0290	3
727	...	274.6515	-13.3889	4152674655836162432	13.73	FH	0.5200	0.0220	-0.1880	0.0250	-1.3610	0.0200	3
728	...	275.8482	-12.9515	41525753270931919616	16.14	FH	0.3270	0.0650	-1.0820	0.0670	-2.4390	0.0560	3
743	...	281.1143	-4.7628	4256653099674779648	12.99	I	0.1790	0.0210	-1.3170	0.0220	-3.5870	0.0180	3
746	...	282.1704	-2.6081	4259014232143657856	13.06	I	1.6060	0.0140	0.3770	0.0150	-6.4960	0.0130	3
748	...	281.9025	-2.0587	4259124282087556096	19.03	H	1.0400	0.2380	-1.0440	0.2500	-24.6100	0.2360	3
750	...	282.8555	-1.9914	4259155721251523328	13.24	I	0.2950	0.0170	-0.9450	0.0180	-2.6700	0.0150	3
762	...	286.8340	+6.4025	430585847961659392384	14.80	I	0.1970	0.0280	-1.5390	0.0300	-3.9310	0.0320	3
764	...	287.5512	+8.2860	430730237356680576	12.15	I	1.7830	0.0170	1.6620	0.0160	-3.1430	0.0160	3
773	...	291.6395	+15.7102	4321568128714147072	14.00	I	0.1980	0.0190	-2.8510	0.0170	-6.2520	0.0160	3
779	HD 344878	296.1836	+23.8522	20205156573166332320	10.27	FH	0.4780	0.0130	-1.7210	0.0080	-5.3880	0.0130	3	(B3)	N95
780	...	298.0551	+26.2532	2027062286983529600	14.24	FB/H	0.2000	0.0180	-2.9220	0.0120	-6.1940	0.0160	3
782	...	307.0810	+37.1849	2057808652171061760	15.29	FH	0.2870	0.0260	-2.7000	0.0240	-3.8970	0.0280	3
784	...	306.2694	+38.6070	2061143299142647936	15.66	H	0.2120	0.0460	-2.5690	0.0440	-4.3080	0.0520	3
789	...	308.7860	+42.4325	2069492028364032128	15.44	FB	0.8770	0.1070	-2.6280	0.1200	-4.1950	0.1310	3
790	...	310.3007	+42.0233	2066375119057281792	16.46	H	0.5200	0.0910	-1.7480	0.1020	-4.6450	0.0950	3
792	BD+57 2513	335.5107	+58.7193	220036745508694774	9.46	H	0.4470	0.0180	3.9150	0.0220	-2.6630	0.0190	3	(O9.5V)	...
793	...	338.5553	+59.2511	2200590922917762176	15.28	FH	0.1000	0.0240	-2.6200	0.0270	-1.3580	0.0250	3
795	...	178.3651	-62.0891	5334731122684318208	12.59	I	0.0970	0.0120	-6.2310	0.0120	2.0950	0.0130	3	(B0)	R03
797	TYC 8978-4428-1	181.8195	-62.55781	6057407744388902656	12.18	I	0.2780	0.0100	-7.8090	0.0090	1.2300	0.0100	3
807	...	199.0394	-62.9448	5862275221161671424	11.70	FH	0.1550	0.0190	-7.0950	0.0140	-0.6740	0.0190	3
809	...	201.4848	-62.5050	5868255567952233344	11.65	I	0.2010	0.0200	-6.2440	0.0160	-1.1730	0.0200	3
826	...	234.2419	-56.8263	5882650434612886400	13.01	I	0.5740	0.0200	-1.6340	0.0200	-3.7750	0.0200	3
828	...	234.6874	-55.8333	5883578671198961664	13.11	H	0.2680	0.0140	-2.7410	0.0140	-3.0950	0.0130	3
834	...	237.7332	-54.2861	5884847541974822400	14.70	I	0.3240	0.0250	-3.2480	0.0240	-3.4560	0.0220	3
838	CPD-53 6825	239.2980	-54.0881	5884771366454491904	10.51	FB/H	0.3290	0.0140	-2.4960	0.0150	-3.5180	0.0120	3	(B0.5lab)	M80
840	...	240.1766	-53.5402	5980842015240024576	12.43	I	0.3680	0.0150	-1.5400	0.0190	-2.6870	0.0150	3
851	...	245.5977	-50.5661	5935235475510713728	13.45	FB/H	0.3120	0.0210	-5.1470	0.0260	-7.4750	0.0190	3
852	...	245.4444	-50.0068	5935302996713445152	18.19	FH	1.0120	0.1490	-3.7160	0.1590	-13.0890	0.1200	3
856	...	247.5132	-49.9379	5940560483366465152	13.95	I	0.1920	0.0190	-2.2140	0.0220	-3.3470	0.0160	3
857	WRAY 15-1506	248.5026	-49.2888	5940705378393686144	11.32	I	0.2410	0.0420	-3.3090	0.0510	-3.1080	0.0350	3
860	...	248.9289	-48.0634	594114349940691936	17.08	H	0.4740	0.0800	-2.5430	0.0800	-6.9410	0.0600	3
863	...	251.3548	-46.1452	594307813189519296	12.59	FB/H	0.2980	0.0210	-2.3440	0.0250	-2.9410	0.0200	3
864	TYC 8326-146-1	250.9237	-45.5034	5943178210070800000	11.10	I	0.2950	0.0180	-1.7360	0.0210	-3.5890	0.0190	3

Table 2 *continued on next page*

Table 2 (*continued*)

SBN ID	Alias	α (2000)	δ (2000)	EDR3 ID	G	Env.	π	σ_π	μ_α	σ_{μ_α}	μ_δ	σ_{μ_δ}	Code	Sp.T.	Ref.
(1)	(2)	(3)	(4)	(5)	(6)	(7)	(8)	(9)	(10)	(11)	(12)	(13)	(14)	(15)	(16)
865	...	250.2864	-44.9649	5943394783836236800	14.13	I	0.1940	0.0270	-6.5130	0.0360	-2.2540	0.0270	3
869	...	253.2755	-44.4957	5964341201877543296	17.61	FB/H	0.6020	0.0940	1.2840	0.1230	-0.9560	0.0940	3
873	...	255.3824	-41.6322	5966392680104284160	16.08	I	0.3280	0.0460	-0.5860	0.0540	1.5510	0.0460	3
876	...	257.0028	-40.5295	5966883169672754304	16.20	FB/H	0.3190	0.0490	-0.9650	0.0610	-3.0320	0.0430	3
880	...	259.7953	-39.0279	5972652822606015360	13.98	I	0.1940	0.0210	-1.1900	0.0270	-3.0130	0.0190	3
884	CD-35 11561	261.63604	-35.1923	5975742450246630144	11.06	I	0.5390	0.0190	-0.8590	0.0210	-2.7470	0.0170	3	(OB ϵ)	S71
885	HD 157642	261.47775	-34.8516	5975823711025599488	8.64	I	5.7060	0.0190	-2.2840	0.0220	-42.2830	0.0160	3	(F5V)	H82
887	HD 319881	262.0903	-34.5418	5975879098930655104	9.56	I	0.5580	0.0170	1.7730	0.0180	-3.2580	0.0130	3	(O6V)	G11
892	V1081 Sco	262.3039	-31.5343	4057914208312575360	6.95	I	0.8230	0.0510	1.7640	0.0520	-1.3370	0.0340	3	(O9.5V)	S14
895	...	264.6345	-29.7186	406006127910676992	11.78	I	0.3400	0.0190	-0.4540	0.0220	-1.8460	0.0150	3

NOTE—References for source of spectral types in Column 18: A16—Alexander et al. (2016); B96—Barnbaum et al. (1996); B18—Berlanas et al. (2018); C93—Cannon & Pickering (1993); G11—Cvavaranadze et al. (2011); H56—Hiltner (1956); H64—Hardorp et al. (1964); H93—Hillenbrand et al. (1993); H75—Honk & Cowley (1975); H78—Honk (1978); H88—Honk (1988); K10—Kobulnicky et al. (2010); M16—Maíz Apellániz et al. (2016); M54—Münch (1954); M95—Massey et al. (1995); N95—Nesterov et al. (1995); P12—Parthasarathy et al. (2012); R03—Reed (2003); R19—Roman-Lopes & Roman-Lopes (2019); S11—Sota et al. (2011); S14—Sota et al. (2014); S17—Sana et al. (2017); S60—Stock et al. (1960); S71—Stephenson & Sanduleak (1971); V93—Vijapurkar & Drilling (1993); W07—Wolff et al. (2007); W71—Walborn (1971)

Table 3. Kinematic Data for SBN Central Stars

SBN ID	v_{2D}	σ_{2D}	v_{3D}	σ_{3D}	PA_m	PA_k	σ_{PA_k}	$\Delta_{PA(m-k)}$	σ_Δ	Code
	(km s $^{-1}$)	(deg.)	(deg.)	(deg.)	(deg.)	(deg.)				
(1)	(2)	(3)	(4)	(5)	(6)	(7)	(8)	(9)	(10)	(11)
1	19	2	-999	-999	27	89	9	-62	12	3
2	19	4	-999	-999	145	236	11	-91	14	3
3	83	8	-999	-999	200	193	1	7	8	3
7	11	1	-999	-999	25	63	11	-38	14	3
10	19	2	-999	-999	140	130	13	10	15	3
12	32	3	-999	-999	180	182	4	-2	9	3
14	20	33	-999	-999	210	225	22	-15	24	3
16	5	2	-999	-999	65	27	41	38	42	3
17	12	3	-999	-999	350	225	23	125	25	3
18	3	11	-999	-999	50	188	63	-138	63	3
19	26	2	-999	-999	290	302	6	-12	10	3
26	8	2	-999	-999	30	37	6	-7	10	3
27	6	2	-999	-999	60	28	86	32	86	3
28	28	3	-999	-999	125	188	5	-63	9	3
29	6	2	-999	-999	85	33	16	52	18	3
32	20	3	-999	-999	20	207	6	173	10	3
36	20	50	-999	-999	355	91	24	-96	26	3
37	12	2	-999	-999	95	85	18	10	20	3
39	65	4	-999	-999	260	244	2	16	8	3
45	28	3	-999	-999	245	179	12	66	14	3
51	3	1	-999	-999	140	8	40	132	41	3
54	17	2	17	8	260	294	9	-34	12	1
63	5	1	-999	-999	300	35	47	-95	47	3
64	55	2	-999	-999	120	115	3	5	9	3
65	3	1	-999	-999	330	11	47	-41	48	3
66	23	1	-999	-999	320	309	6	11	10	3
67	4	1	-999	-999	300	15	32	-75	33	3
83	10	3	11	20	69	256	16	173	18	2
89	2	2	-999	-999	110	330	25	140	26	3
101	9	1	-999	-999	305	80	24	-134	25	3
129	11	2	-999	-999	100	30	4	70	9	3
157	45	15	-999	-999	315	29	2	-74	8	3
163	6	5	-999	-999	260	267	42	-7	43	3
165	21	17	-999	-999	10	21	5	-11	9	3
173	13	15	-999	-999	40	268	39	132	39	3
195	10	23	-999	-999	220	24	117	-164	118	3
197	15	26	-999	-999	345	11	21	-26	23	3
200	34	13	44	14	260	30	2	-130	8	2
203	13	2	-999	-999	25	132	21	-107	22	3
212	15	1	25	12	115	114	14	1	16	1
240	8	2	24	3	238	333	9	-95	12	2
249	14	4	21	7	235	298	18	-63	20	2
252	15	2	-999	-999	237	144	32	93	33	3
255	19	2	28	3	10	24	3	-14	8	2
263	44	12	-999	-999	80	75	6	5	10	3
265	17	5	44	7	5	32	4	-27	9	2
268	13	1	-999	-999	310	161	11	149	14	3

Table 3 continued on next page

Table 3 (*continued*)

SBN ID	v_{2D}	σ_{2D}	v_{3D}	σ_{3D}	PA_m	PA_k	σ_{PA_k}	$\Delta_{PA(m-k)}$	σ_Δ	Code
	(km s $^{-1}$)	(deg.)	(deg.)	(deg.)	(deg.)	(deg.)				
(1)	(2)	(3)	(4)	(5)	(6)	(7)	(8)	(9)	(10)	(11)
271	16	5	45	14	29	48	6	-19	10	2
272	60	18	63	27	260	277	10	-17	13	1
282	42	8	55	8	45	39	2	6	8	2
284	32	12	35	16	140	316	20	-176	22	2
285	35	7	47	11	340	8	4	-28	9	1
287	10	4	-999	-999	117	213	40	-96	41	3
288	11	2	38	18	320	229	6	91	10	2
289	12	1	-999	-999	290	284	8	6	11	3
291	13	20	-999	-999	25	197	9	-172	12	3
295	3	2	-999	-999	352	287	28	65	29	3
296	7	23	-999	-999	355	234	18	121	20	3
298	25	2	35	2	170	144	6	26	10	2
300	4	1	16	2	189	206	101	-17	101	2
303	52	90	55	90	10	209	11	161	14	1
306	7	1	14	5	270	70	42	-160	43	2
309	15	83	-999	-999	165	202	44	-37	44	3
313	6	2	-999	-999	169	261	10	-92	13	3
314	11	2	-999	-999	285	222	5	62	9	3
315	37	42	-999	-999	215	206	10	9	13	3
318	9	2	-999	-999	38	241	5	157	9	3
319	11	12	37	45	91	164	45	-73	46	1
320	7	2	9	2	290	53	56	-123	56	2
321	1	1	18	2	35	258	16	137	18	2
322	3	1	14	19	35	247	28	148	29	1
324	30	2	36	4	225	286	4	-61	9	2
326	17	2	22	3	100	70	6	30	10	2
328	18	1	20	15	130	111	8	19	11	2
329	38	2	46	4	225	202	2	23	8	2
330	9	1	39	2	40	172	12	-132	14	2
331	4	2	25	30	20	248	7	132	11	1
332	5	1	43	20	140	297	12	-157	14	1
333	2	1	10	2	210	285	16	-75	17	3
335	12	2	15	2	205	32	7	174	10	2
336	26	2	-999	-999	90	147	4	-57	9	3
338	4	2	4	8	290	313	22	-23	23	2
339	77	3	88	10	70	44	1	26	8	2
340	19	2	25	3	100	48	4	52	9	2
341	11	2	36	10	135	4	10	131	13	1
342	14	2	14	5	350	330	6	20	10	2
343	49	2	123	12	340	358	2	-18	8	2
344	45	2	-999	-999	10	356	2	14	8	3
345	6	2	32	2	70	327	25	103	26	2
346	15	2	216	9	0	34	6	-34	10	1
349	20	2	31	6	245	227	2	18	8	2
351	6	20	10	20	330	230	17	100	18	2
352	5	2	7	5	270	309	23	-39	25	2
353	67	4	70	5	265	286	1	-21	8	2
354	8	4	11	5	115	221	30	-106	31	3
356	10	2	38	18	45	10	17	35	19	1
358	2	1	14	2	300	264	10	36	13	2

Table 3 *continued on next page*

Table 3 (*continued*)

SBN ID	v_{2D}	σ_{2D}	v_{3D}	σ_{3D}	PA_m	PA_k	σ_{PA_k}	$\Delta_{PA(m-k)}$	σ_Δ	Code
	(km s $^{-1}$)	(deg.)	(deg.)	(deg.)	(deg.)	(deg.)				
(1)	(2)	(3)	(4)	(5)	(6)	(7)	(8)	(9)	(10)	(11)
359	12	2	59	3	170	78	26	92	28	2
360	74	4	103	8	220	226	1	-6	8	1
361	29	2	45	9	50	54	3	-4	8	1
362	27	2	27	11	95	74	3	20	9	2
365	11	2	13	2	145	178	34	-33	35	2
366	11	2	-999	-999	5	359	12	6	14	3
367	8	2	35	2	45	7	28	38	29	2
368	8	1	-999	-999	269	271	14	-2	16	3
371	24	3	11	37	220	201	10	19	13	1
372	16	2	86	111	325	256	9	69	12	1
373	23	3	-999	-999	300	308	2	-8	8	3
374	18	2	-999	-999	315	298	7	18	11	3
375	88	3	-999	-999	350	354	1	-4	8	3
376	21	2	-999	-999	50	28	5	22	9	3
377	42	2	-999	-999	20	286	3	94	9	3
378	9	2	-999	-999	45	207	24	-162	25	3
381	11	3	-999	-999	340	346	6	-6	10	3
383	88	13	-999	-999	310	319	1	-9	8	3
384	4	2	-999	-999	45	128	9	-83	12	3
385	30	2	-999	-999	348	359	3	-11	8	3
386	48	2	-999	-999	345	5	2	-20	8	3
389	15	1	-999	-999	285	234	11	51	14	3
390	20	2	-999	-999	315	307	4	8	9	3
391	10	1	-999	-999	10	174	7	-164	11	3
393	9	1	-999	-999	300	167	7	133	10	3
394	57	2	-999	-999	135	138	1	-3	8	3
395	11	1	-999	-999	210	168	6	42	10	3
396	27	2	-999	-999	90	98	3	-8	9	3
397	31	2	-999	-999	315	286	2	29	8	3
404	17	2	-999	-999	100	124	2	-24	8	3
405	11	2	-999	-999	355	340	15	15	17	3
406	12	2	-999	-999	110	197	18	-87	20	3
407	10	2	-999	-999	205	129	4	76	9	3
408	4	1	-999	-999	325	118	8	-153	11	3
409	19	2	-999	-999	20	200	8	-180	11	3
410	14	1	-999	-999	5	180	10	-175	13	3
411	5	1	-999	-999	220	111	5	109	9	3
412	4	1	-999	-999	340	116	10	-136	12	3
414	7	1	-999	-999	310	132	28	178	29	3
422	9	2	-999	-999	100	109	4	-9	9	3
425	17	2	-999	-999	100	117	3	-17	9	3
426	15	2	-999	-999	200	109	3	91	9	3
430	10	1	-999	-999	260	125	9	135	12	3
431	9	1	-999	-999	80	50	5	30	9	3
434	76	4	-999	-999	95	97	1	-2	8	3
440	11	31	-999	-999	85	140	71	-55	72	3
445	6	7	-999	-999	270	88	36	-178	37	3
448	6	3	-999	-999	35	68	5	-33	10	3
449	11	3	-999	-999	205	100	4	104	9	3
450	9	5	-999	-999	280	121	98	159	99	3

Table 3 *continued on next page*

Table 3 (*continued*)

SBN ID	v_{2D}	σ_{2D}	v_{3D}	σ_{3D}	PA_m	PA_k	σ_{PA_k}	$\Delta_{PA(m-k)}$	σ_Δ	Code
	(km s $^{-1}$)	(deg.)	(deg.)	(deg.)	(deg.)	(deg.)				
(1)	(2)	(3)	(4)	(5)	(6)	(7)	(8)	(9)	(10)	(11)
453	11	2	-999	-999	350	97	4	-107	9	3
458	14	4	-999	-999	195	81	4	114	9	3
462	14	1	-999	-999	155	128	8	27	12	3
463	8	2	-999	-999	300	107	34	-167	35	3
464	9	1	-999	-999	170	110	11	60	13	3
467	3	1	-999	-999	345	42	10	-57	12	3
468	11	7	-999	-999	345	82	21	-97	23	3
469	10	2	-999	-999	110	260	99	-150	99	3
470	13	2	-999	-999	85	186	41	-101	41	3
471	10	2	-999	-999	175	322	58	-147	59	3
473	7	2	-999	-999	325	359	16	-34	18	3
474	18	2	-999	-999	280	280	8	-0	11	3
484	26	3	-999	-999	325	263	7	62	11	3
485	7	2	-999	-999	5	74	4	-69	9	3
489	38	7	-999	-999	35	80	1	-45	8	3
497	8	1	-999	-999	265	7	10	-102	13	3
506	11	2	-999	-999	245	212	95	33	95	3
509	18	10	-999	-999	25	31	9	-6	12	3
512	20	6	-999	-999	220	141	22	79	24	3
513	11	2	-999	-999	140	270	62	-130	63	3
514	21	2	-999	-999	215	188	11	27	14	3
515	38	2	-999	-999	235	232	2	3	8	3
517	20	2	-999	-999	160	207	15	-47	17	3
518	7	2	-999	-999	65	41	68	24	68	3
520	17	14	-999	-999	180	57	5	123	10	3
534	5	3	-999	-999	120	3	21	117	22	3
539	33	10	-999	-999	0	89	9	-89	12	3
544	38	3	-999	-999	225	218	2	7	8	3
545	2	14	-999	-999	155	216	115	-61	115	3
548	10	12	-999	-999	280	33	38	-113	39	3
555	14	2	-999	-999	290	321	9	-31	12	3
558	16	3	-999	-999	225	144	36	81	37	3
561	17	5	-999	-999	145	46	4	98	9	3
575	95	9	-999	-999	195	194	1	0	8	3
579	13	3	-999	-999	250	290	15	-40	17	3
581	13	3	-999	-999	250	282	18	-32	19	3
583	24	3	-999	-999	290	233	4	57	9	3
584	21	3	-999	-999	90	194	11	-104	14	3
587	4	12	-999	-999	235	46	112	-172	113	3
589	10	2	-999	-999	350	312	18	38	20	3
607	22	6	-999	-999	175	211	39	-36	40	3
614	7	3	-999	-999	45	55	50	-10	51	3
616	45	4	-999	-999	280	218	4	62	9	3
618	17	4	-999	-999	230	158	20	72	22	3
619	44	7	-999	-999	290	230	25	60	26	3
624	28	3	-999	-999	25	215	4	170	9	3
626	3	2	-999	-999	5	12	7	-7	11	3
634	9	2	-999	-999	350	75	44	-85	45	3
635	6	3	-999	-999	55	18	6	38	10	3
636	21	3	-999	-999	80	214	6	-134	10	3

Table 3 *continued on next page*

Table 3 (*continued*)

SBN ID	v_{2D}	σ_{2D}	v_{3D}	σ_{3D}	PA_m	PA_k	σ_{PA_k}	$\Delta_{PA(m-k)}$	σ_Δ	Code
	(km s $^{-1}$)	(deg.)	(deg.)	(deg.)	(deg.)	(deg.)				
(1)	(2)	(3)	(4)	(5)	(6)	(7)	(8)	(9)	(10)	(11)
641	25	4	-999	-999	100	218	13	-118	15	3
648	48	20	-999	-999	180	206	40	-26	41	3
653	15	2	-999	-999	225	171	23	54	25	3
655	25	3	-999	-999	305	217	4	88	9	3
656	34	3	-999	-999	280	218	2	62	8	3
657	24	3	-999	-999	255	210	10	45	13	3
662	13	3	-999	-999	70	25	3	45	9	3
667	29	2	-999	-999	120	120	7	-0	10	3
670	33	3	-999	-999	140	232	3	-92	8	3
673	21	3	-999	-999	130	227	5	-97	10	3
681	9	2	-999	-999	120	91	80	29	80	3
687	20	3	-999	-999	105	191	9	-86	12	3
691	15	2	-999	-999	25	286	11	99	14	3
692	17	1	-999	-999	55	96	11	-41	14	3
700	16	3	-999	-999	105	206	18	-101	19	3
701	15	3	-999	-999	180	232	15	-52	17	3
705	24	3	-999	-999	160	226	4	-66	9	3
709	22	2	-999	-999	115	139	11	-24	13	3
712	17	4	-999	-999	63	19	3	44	9	3
713	4	2	-999	-999	51	21	36	30	37	3
714	8	2	-999	-999	351	64	36	-73	36	3
715	5	3	-999	-999	29	4	7	25	11	3
717	7	1	-999	-999	60	54	24	6	25	3
718	34	3	-999	-999	170	192	3	-22	9	3
720	17	2	-999	-999	38	176	15	-138	17	3
722	5	2	-999	-999	45	23	74	22	74	3
723	39	61	-999	-999	170	156	63	14	64	3
727	1	2	-999	-999	148	345	20	163	21	3
728	10	12	-999	-999	156	241	24	-85	25	3
743	9	23	-999	-999	340	36	20	-56	22	3
746	10	2	-999	-999	144	200	30	-56	32	3
748	92	34	-999	-999	195	184	1	11	8	3
750	8	3	-999	-999	343	16	8	-33	11	3
762	29	18	-999	-999	104	31	3	73	9	3
764	5	2	-999	-999	144	14	30	130	31	3
773	17	3	-999	-999	208	199	7	9	11	3
779	8	1	-999	-999	137	157	28	-20	29	3
780	16	2	-999	-999	210	183	6	27	10	3
782	21	3	-999	-999	95	12	4	83	9	3
784	18	7	-999	-999	358	35	24	-37	25	3
789	3	2	-999	-999	340	291	16	49	18	3
790	12	4	-999	-999	169	81	21	88	23	3
792	4	2	-999	-999	354	270	6	84	10	3
793	23	38	-999	-999	1	266	23	95	25	3
795	50	25	-999	-999	356	331	15	25	17	3
797	21	2	-999	-999	278	308	5	-30	9	3
807	11	4	-999	-999	11	347	18	24	19	3
809	6	4	-999	-999	81	78	6	3	10	3
826	12	1	-999	-999	226	88	7	138	11	3
828	12	2	-999	-999	99	74	4	25	9	3

Table 3 *continued on next page*

Table 3 (*continued*)

SBN ID	v_{2D}	σ_{2D}	v_{3D}	σ_{3D}	PA_m	PA_k	σ_{PA_k}	$\Delta_{PA(m-k)}$	σ_Δ	Code
	(km s $^{-1}$)	(deg.)	(deg.)	(deg.)	(deg.)	(deg.)				
(1)	(2)	(3)	(4)	(5)	(6)	(7)	(8)	(9)	(10)	(11)
834	15	2	-999	-999	174	225	42	-51	43	3
838	13	2	-999	-999	61	133	22	-72	24	3
840	10	2	-999	-999	65	64	4	2	9	3
851	91	5	-999	-999	231	214	1	17	8	3
852	47	9	-999	-999	325	190	3	134	8	3
856	8	11	-999	-999	39	67	27	-28	29	3
857	27	9	-999	-999	271	266	27	5	28	3
860	50	10	-999	-999	241	195	3	46	8	3
863	24	3	-999	-999	102	245	5	-143	9	3
864	29	3	-999	-999	67	197	5	-130	9	3
865	106	6	-999	-999	116	279	9	-163	12	3
869	16	4	-999	-999	170	48	5	122	9	3
873	40	8	-999	-999	216	4	3	-148	8	3
876	26	4	-999	-999	259	195	10	64	12	3
880	34	6	-999	-999	40	196	25	-156	26	3
884	16	3	-999	-999	218	225	11	-7	14	3
885	26	3	-999	-999	78	182	6	-104	10	3
887	24	1	-999	-999	123	121	9	2	12	3
892	10	2	-999	-999	57	51	7	6	10	3
895	18	3	-999	-999	229	214	6	15	10	3

Table 4. Summary of Principal Conclusions

Property	Value
Galactic O Star Catalog Findings	
Overall Runaway Fraction	22_{-3}^{+3}
Multiplicity fraction among 25 runaways	>28%
16th/50th/84th percentiles of v_{2D}	5.6/11.4/32.6 km s $^{-1}$
Bowshock Nebula Central Star Findings	
Runaway Fraction	$24_{-7}^{+9}\%$
Multiplicity Fraction	>36% \pm 6%
16th/50th/84th percentiles of v_{2D}	6.5/14.6/32.6 km s $^{-1}$

REFERENCES

- Acreman, D. M., Stevens, I. R., & Harries, T. J. 2016, MNRAS, 456, 136, doi: [10.1093/mnras/stv2632](https://doi.org/10.1093/mnras/stv2632)
- Alexander, M. J., Hanes, R. J., Povich, M. S., & McSwain, M. V. 2016, AJ, 152, 190, doi: [10.3847/0004-6256/152/6/190](https://doi.org/10.3847/0004-6256/152/6/190)
- Astropy Collaboration, Robitaille, T. P., Tollerud, E. J., et al. 2013, A&A, 558, A33, doi: [10.1051/0004-6361/201322068](https://doi.org/10.1051/0004-6361/201322068)
- Aumer, M., & Binney, J. J. 2009, MNRAS, 397, 1286, doi: [10.1111/j.1365-2966.2009.15053.x](https://doi.org/10.1111/j.1365-2966.2009.15053.x)
- Bally, J., Sutherland, R. S., Devine, D., & Johnstone, D. 1998, AJ, 116, 293, doi: [10.1086/300399](https://doi.org/10.1086/300399)
- Banyard, G., Sana, H., Mahy, L., et al. 2022, A&A, 658, A69, doi: [10.1051/0004-6361/202141037](https://doi.org/10.1051/0004-6361/202141037)
- Barannikov, A. A. 1993, Astronomy Letters, 19, 420
- Barnbaum, C., Stone, R. P. S., & Keenan, P. C. 1996, ApJS, 105, 419, doi: [10.1086/192323](https://doi.org/10.1086/192323)
- Berlanas, S. R., Herrero, A., Comerón, F., et al. 2018, A&A, 612, A50, doi: [10.1051/0004-6361/201731856](https://doi.org/10.1051/0004-6361/201731856)
- Blaauw, A. 1961, Bulletin of the Astronomical Institutes of the Netherlands, 15, 265
- Bobylev, V. V., & Bajkova, A. T. 2007, Astronomy Reports, 51, 372, doi: [10.1134/S1063772907050034](https://doi.org/10.1134/S1063772907050034)
- Bodenheimer, P., Tenorio-Tagle, G., & Yorke, H. W. 1979, ApJ, 233, 85, doi: [10.1086/157368](https://doi.org/10.1086/157368)
- Bodensteiner, J., Baade, D., Greiner, J., & Langer, N. 2018, A&A, 618, A110, doi: [10.1051/0004-6361/201832722](https://doi.org/10.1051/0004-6361/201832722)
- Brown, D., & Bomans, D. J. 2005, A&A, 439, 183, doi: [10.1051/0004-6361:20041054](https://doi.org/10.1051/0004-6361:20041054)
- Cannon, A. J., & Pickering, E. C. 1993, VizieR Online Data Catalog, III/135A
- Cantat-Gaudin, T., & Brandt, T. D. 2021, A&A, 649, A124, doi: [10.1051/0004-6361/202140807](https://doi.org/10.1051/0004-6361/202140807)
- Castaneda, H. O. 1988, ApJS, 67, 93, doi: [10.1086/191268](https://doi.org/10.1086/191268)
- Chick, W. T., Kobulnicky, H. A., Schurhammer, D. P., et al. 2020, ApJS, 251, 29, doi: [10.3847/1538-4365/abc0e5](https://doi.org/10.3847/1538-4365/abc0e5)
- Chick, W. T. W. 2020, PhD thesis, University of Wyoming
- Clemens, D. P., Sanders, D. B., & Scoville, N. Z. 1988, ApJ, 327, 139, doi: [10.1086/166177](https://doi.org/10.1086/166177)
- Comeron, F., & Kaper, L. 1998, A&A, 338, 273
- Cruz-González, C., Recillas-Cruz, E., Costero, R., Peimbert, M., & Torres-Peimbert, S. 1974, RMxAA, 1, 211
- Dale, J. E., Ercolano, B., & Bonnell, I. A. 2012, Monthly Notices of the Royal Astronomical Society, 424, 377, doi: [10.1111/j.1365-2966.2012.21205.x](https://doi.org/10.1111/j.1365-2966.2012.21205.x)
- De Donder, E., Vanbeveren, D., & van Bever, J. 1997, A&A, 318, 812
- de la Fuente Marcos, R., & de la Fuente Marcos, C. 2018, Research Notes of the American Astronomical Society, 2, 35, doi: [10.3847/2515-5172/aac5d7](https://doi.org/10.3847/2515-5172/aac5d7)
- de Wit, W. J., Testi, L., Palla, F., & Zinnecker, H. 2005, A&A, 437, 247, doi: [10.1051/0004-6361:20042489](https://doi.org/10.1051/0004-6361:20042489)
- Dehnen, W., & Binney, J. J. 1998, MNRAS, 298, 387, doi: [10.1046/j.1365-8711.1998.01600.x](https://doi.org/10.1046/j.1365-8711.1998.01600.x)
- Ding, P.-J., Zhu, Z., & Liu, J.-C. 2019, Research in Astronomy and Astrophysics, 19, 068, doi: [10.1088/1674-4527/19/5/68](https://doi.org/10.1088/1674-4527/19/5/68)
- Drew, J. E., Herrero, A., Mohr-Smith, M., et al. 2018, MNRAS, 480, 2109, doi: [10.1093/mnras/sty1905](https://doi.org/10.1093/mnras/sty1905)
- Eldridge, J. J., Langer, N., & Tout, C. A. 2011, MNRAS, 414, 3501, doi: [10.1111/j.1365-2966.2011.18650.x](https://doi.org/10.1111/j.1365-2966.2011.18650.x)
- Evans, F. A., Renzo, M., & Rossi, E. M. 2020, MNRAS, 497, 5344, doi: [10.1093/mnras/staa2334](https://doi.org/10.1093/mnras/staa2334)
- Fullerton, A. W., Gies, D. R., & Bolton, C. T. 1996, ApJS, 103, 475, doi: [10.1086/192285](https://doi.org/10.1086/192285)
- Gaia Collaboration, Brown, A. G. A., Vallenari, A., et al. 2016a, A&A, 595, A2, doi: [10.1051/0004-6361/201629512](https://doi.org/10.1051/0004-6361/201629512)

- Gaia Collaboration, Prusti, T., de Bruijne, J. H. J., et al. 2016b, A&A, 595, A1, doi: [10.1051/0004-6361/201629272](https://doi.org/10.1051/0004-6361/201629272)
- Gaia Collaboration, Brown, A. G. A., Vallenari, A., et al. 2018, A&A, 616, A1, doi: [10.1051/0004-6361/201833051](https://doi.org/10.1051/0004-6361/201833051)
- Gaia Collaboration, Klioner, S. A., Mignard, F., et al. 2021, A&A, 649, A9, doi: [10.1051/0004-6361/202039734](https://doi.org/10.1051/0004-6361/202039734)
- Gao, Y., Li, J., & Jia, S. 2019, MNRAS, 487, 3178, doi: [10.1093/mnras/stz1525](https://doi.org/10.1093/mnras/stz1525)
- Gáspár, A., Su, K. Y. L., Rieke, G. H., et al. 2008, ApJ, 672, 974, doi: [10.1086/523299](https://doi.org/10.1086/523299)
- Gies, D. R., & Bolton, C. T. 1986, ApJS, 61, 419, doi: [10.1086/191118](https://doi.org/10.1086/191118)
- Golubov, O., Just, A., Bienaymé, O., et al. 2013, A&A, 557, A92, doi: [10.1051/0004-6361/201321559](https://doi.org/10.1051/0004-6361/201321559)
- Goodwin, S. P., & Bastian, N. 2006, Monthly Notices of the Royal Astronomical Society, 373, 752, doi: [10.1111/j.1365-2966.2006.11078.x](https://doi.org/10.1111/j.1365-2966.2006.11078.x)
- Gull, T. R., & Sofia, S. 1979, ApJ, 230, 782, doi: [10.1086/157137](https://doi.org/10.1086/157137)
- Gvaramadze, V. V., & Bomans, D. J. 2008, A&A, 490, 1071, doi: [10.1051/0004-6361:200810411](https://doi.org/10.1051/0004-6361:200810411)
- Gvaramadze, V. V., Miroshnichenko, A. S., Castro, N., Langer, N., & Zharikov, S. V. 2014, MNRAS, 437, 2761, doi: [10.1093/mnras/stt2087](https://doi.org/10.1093/mnras/stt2087)
- Gvaramadze, V. V., Röser, S., Scholz, R. D., & Schilbach, E. 2011, A&A, 529, A14, doi: [10.1051/0004-6361/201016256](https://doi.org/10.1051/0004-6361/201016256)
- Hardorp, J., Theile, I., & Voigt, H. H. 1964, Hamburger Sternw. Warner & Swasey Obs., C03, 0
- Henney, W. J., & Arthur, S. J. 2019, MNRAS, 486, 3423, doi: [10.1093/mnras/stz1043](https://doi.org/10.1093/mnras/stz1043)
- Hillenbrand, L. A., Massey, P., Strom, S. E., & Merrill, K. M. 1993, AJ, 106, 1906, doi: [10.1086/116774](https://doi.org/10.1086/116774)
- Hills, J. G. 1980, The Astrophysical Journal, 235, 986, doi: [10.1086/157703](https://doi.org/10.1086/157703)
- Hiltner, W. A. 1956, ApJS, 2, 389, doi: [10.1086/190029](https://doi.org/10.1086/190029)
- Høg, E., Fabricius, C., Makarov, V. V., et al. 2000, A&A, 355, L27
- Hoogerwerf, R., de Bruijne, J. H. J., & de Zeeuw, P. T. 2000, ApJL, 544, L133, doi: [10.1086/317315](https://doi.org/10.1086/317315)
- . 2001, A&A, 365, 49, doi: [10.1051/0004-6361:20000014](https://doi.org/10.1051/0004-6361:20000014)
- Houk, N. 1978, Michigan catalogue of two-dimensional spectral types for the HD stars
- Houk, N., & Cowley, A. P. 1975, University of Michigan Catalogue of two-dimensional spectral types for the HD stars. Volume I. Declinations -90° to -53°f0.
- Irrgang, A., Wilcox, B., Tucker, E., & Schiefelbein, L. 2013, A&A, 549, A137, doi: [10.1051/0004-6361/201220540](https://doi.org/10.1051/0004-6361/201220540)
- Jayasinghe, T., Dixon, D., Povich, M. S., et al. 2019, MNRAS, 488, 1141, doi: [10.1093/mnras/stz1738](https://doi.org/10.1093/mnras/stz1738)
- Johnson, D. R. H., & Soderblom, D. R. 1987, AJ, 93, 864, doi: [10.1086/114370](https://doi.org/10.1086/114370)
- Kobulnicky, H. A., Chick, W. T., & Povich, M. S. 2018, ApJ, 856, 74, doi: [10.3847/1538-4357/aab3e0](https://doi.org/10.3847/1538-4357/aab3e0)
- Kobulnicky, H. A., Gilbert, I. J., & Kiminki, D. C. 2010, ApJ, 710, 549, doi: [10.1088/0004-637X/710/1/549](https://doi.org/10.1088/0004-637X/710/1/549)
- Kobulnicky, H. A., Kiminki, D. C., Lundquist, M. J., et al. 2014, ApJS, 213, 34, doi: [10.1088/0067-0049/213/2/34](https://doi.org/10.1088/0067-0049/213/2/34)
- Kobulnicky, H. A., Chick, W. T., Schurhammer, D. P., et al. 2016, ApJS, 227, 18, doi: [10.3847/0067-0049/227/2/18](https://doi.org/10.3847/0067-0049/227/2/18)
- Lamb, J. B., Oey, M. S., Segura-Cox, D. M., et al. 2016, ApJ, 817, 113, doi: [10.3847/0004-637X/817/2/113](https://doi.org/10.3847/0004-637X/817/2/113)
- Lindgren, L., Hernández, J., Bombrun, A., et al. 2018, A&A, 616, A2, doi: [10.1051/0004-6361/201832727](https://doi.org/10.1051/0004-6361/201832727)
- Lindgren, L., Bastian, U., Biermann, M., et al. 2021, A&A, 649, A4, doi: [10.1051/0004-6361/202039653](https://doi.org/10.1051/0004-6361/202039653)
- Mac Low, M.-M., van Buren, D., Wood, D. O. S., & Churchwell, E. 1991, ApJ, 369, 395, doi: [10.1086/169769](https://doi.org/10.1086/169769)
- Maíz Apellániz, J., Pantaleoni González, M., & Barbá, R. H. 2021, A&A, 649, A13, doi: [10.1051/0004-6361/202140418](https://doi.org/10.1051/0004-6361/202140418)
- Maíz Apellániz, J., Pantaleoni González, M., Barbá, R. H., et al. 2018, A&A, 616, A149, doi: [10.1051/0004-6361/201832787](https://doi.org/10.1051/0004-6361/201832787)
- Maíz Apellániz, J., Pantaleoni González, M., Barbá, R. H., & Weiler, M. 2022, A&A, 657, A72, doi: [10.1051/0004-6361/202142366](https://doi.org/10.1051/0004-6361/202142366)
- Maíz Apellániz, J., Sota, A., Morrell, N. I., et al. 2013, in Massive Stars: From alpha to Omega, 198. <https://arxiv.org/abs/1306.6417>
- Maíz Apellániz, J., Sota, A., Arias, J. I., et al. 2016, ApJS, 224, 4, doi: [10.3847/0067-0049/224/1/4](https://doi.org/10.3847/0067-0049/224/1/4)
- Maíz Apellániz, J., Trigueros Páez, E., Negueruela, I., et al. 2019, A&A, 626, A20, doi: [10.1051/0004-6361/201935359](https://doi.org/10.1051/0004-6361/201935359)
- Markwardt, C. B. 2009, Astronomical Society of the Pacific Conference Series, Vol. 411, Non-linear Least-squares Fitting in IDL with MPFIT, ed. D. A. Bohlender, D. Durand, & P. Dowler, 251
- Mason, B. D., Gies, D. R., Hartkopf, W. I., et al. 1998, AJ, 115, 821, doi: [10.1086/300234](https://doi.org/10.1086/300234)
- Massey, P., Johnson, K. E., & Degioia-Eastwood, K. 1995, ApJ, 454, 151, doi: [10.1086/176474](https://doi.org/10.1086/176474)
- Mayor, M. 1974, A&A, 32, 321
- McSwain, M. V., Boyajian, T. S., Grundstrom, E. D., & Gies, D. R. 2007, ApJ, 655, 473, doi: [10.1086/509914](https://doi.org/10.1086/509914)
- Meyer, D. M. A., Mackey, J., Langer, N., et al. 2014, MNRAS, 444, 2754, doi: [10.1093/mnras/stu1629](https://doi.org/10.1093/mnras/stu1629)
- Meyer, D. M. A., van Marle, A. J., Kuiper, R., & Kley, W. 2016, MNRAS, 459, 1146, doi: [10.1093/mnras/stw651](https://doi.org/10.1093/mnras/stw651)

- Münch, L. 1954, Boletin de los Observatorios Tonantzintla y Tacubaya, 1, 29
- Nesterov, V. V., Kuzmin, A. V., Ashimbaeva, N. T., et al. 1995, *A&AS*, 110, 367
- Noriega-Crespo, A., van Buren, D., & Dgani, R. 1997, *AJ*, 113, 780, doi: [10.1086/118298](https://doi.org/10.1086/118298)
- Ochsendorf, B. B., Cox, N. L. J., Krijt, S., et al. 2014a, *A&A*, 563, A65, doi: [10.1051/0004-6361/201322873](https://doi.org/10.1051/0004-6361/201322873)
- Ochsendorf, B. B., Verdolini, S., Cox, N. L. J., et al. 2014b, *A&A*, 566, A75, doi: [10.1051/0004-6361/201423545](https://doi.org/10.1051/0004-6361/201423545)
- Oey, M. S., Dorigo Jones, J., Castro, N., et al. 2018, *ApJ*, 867, L8, doi: [10.3847/2041-8213/aae892](https://doi.org/10.3847/2041-8213/aae892)
- Oh, S., Kroupa, P., & Pfleiderer-Altenburg, J. 2015, *ApJ*, 805, 92, doi: [10.1088/0004-637X/805/2/92](https://doi.org/10.1088/0004-637X/805/2/92)
- Parthasarathy, M., Drilling, J. S., Vijapurkar, J., & Takeda, Y. 2012, *PASJ*, 64, 57, doi: [10.1093/pasj/64.3.57](https://doi.org/10.1093/pasj/64.3.57)
- Perets, H. B., & Šubr, L. 2012, *ApJ*, 751, 133, doi: [10.1088/0004-637X/751/2/133](https://doi.org/10.1088/0004-637X/751/2/133)
- Peri, C. S., Benaglia, P., Brookes, D. P., Stevens, I. R., & Isequilla, N. L. 2012, *A&A*, 538, A108, doi: [10.1051/0004-6361/201118116](https://doi.org/10.1051/0004-6361/201118116)
- Peri, C. S., Benaglia, P., & Isequilla, N. L. 2015, *A&A*, 578, A45, doi: [10.1051/0004-6361/201424676](https://doi.org/10.1051/0004-6361/201424676)
- Pourbaix, D., Tokovinin, A. A., Batten, A. H., et al. 2004, *A&A*, 424, 727, doi: [10.1051/0004-6361:20041213](https://doi.org/10.1051/0004-6361:20041213)
- Poveda, A., Ruiz, J., & Allen, C. 1967, Boletin de los Observatorios Tonantzintla y Tacubaya, 4, 86
- Povich, M. S., Benjamin, R. A., Whitney, B. A., et al. 2008, *ApJ*, 689, 242, doi: [10.1086/592565](https://doi.org/10.1086/592565)
- Randall, S. K., Bagnulo, S., Ziegerer, E., Geier, S., & Fontaine, G. 2015, *A&A*, 576, A65, doi: [10.1051/0004-6361/201425251](https://doi.org/10.1051/0004-6361/201425251)
- Reed, B. C. 2003, *AJ*, 125, 2531, doi: [10.1086/374771](https://doi.org/10.1086/374771)
- Reid, M. J., & Brunthaler, A. 2004, *ApJ*, 616, 872, doi: [10.1086/424960](https://doi.org/10.1086/424960)
- Reid, M. J., Menten, K. M., Brunthaler, A., et al. 2019, *ApJ*, 885, 131, doi: [10.3847/1538-4357/ab4a11](https://doi.org/10.3847/1538-4357/ab4a11)
- Renzo, M., Zapartas, E., de Mink, S. E., et al. 2019, *A&A*, 624, A66, doi: [10.1051/0004-6361/201833297](https://doi.org/10.1051/0004-6361/201833297)
- Roman-Lopes, A. 2013, *MNRAS*, 435, L73, doi: [10.1093/mnrasl/slt100](https://doi.org/10.1093/mnrasl/slt100)
- Roman-Lopes, A., & Roman-Lopes, G. F. 2019, *MNRAS*, 484, 5578, doi: [10.1093/mnras/stz064](https://doi.org/10.1093/mnras/stz064)
- Rubin, V. C., Burley, J., Kiasatpoor, A., et al. 1962, *AJ*, 67, 491, doi: [10.1086/108758](https://doi.org/10.1086/108758)
- Sana, H., Ramírez-Tannus, M. C., de Koter, A., et al. 2017, *A&A*, 599, L9, doi: [10.1051/0004-6361/201630087](https://doi.org/10.1051/0004-6361/201630087)
- Schönrich, R., Binney, J., & Dehnen, W. 2010, *MNRAS*, 403, 1829, doi: [10.1111/j.1365-2966.2010.16253.x](https://doi.org/10.1111/j.1365-2966.2010.16253.x)
- Sota, A., Maíz Apellániz, J., Morrell, N. I., et al. 2014, *ApJS*, 211, 10, doi: [10.1088/0067-0049/211/1/10](https://doi.org/10.1088/0067-0049/211/1/10)
- Sota, A., Maíz Apellániz, J., Walborn, N. R., et al. 2011, *ApJS*, 193, 24, doi: [10.1088/0067-0049/193/2/24](https://doi.org/10.1088/0067-0049/193/2/24)
- Spierauskas, J., Bartašiūtė, S., Boyle, R. P., et al. 2016, *A&A*, 596, A116, doi: [10.1051/0004-6361/201527850](https://doi.org/10.1051/0004-6361/201527850)
- Spitzer, L. J., & Mathieu, R. D. 1980, *ApJ*, 241, 618, doi: [10.1086/158376](https://doi.org/10.1086/158376)
- Stephenson, C. B., & Sanduleak, N. 1971, Publications of the Warner & Swasey Observatory, 1, 1
- Stock, J., Nassau, J. J., & Stephenson, C. B. 1960, Hamburger Sternw. Warner & Swasey Obs., C02, 0
- Stone, R. C. 1979, *ApJ*, 232, 520, doi: [10.1086/157311](https://doi.org/10.1086/157311)
- . 1991, *AJ*, 102, 333, doi: [10.1086/115880](https://doi.org/10.1086/115880)
- Tenorio-Tagle, G. 1979, *A&A*, 71, 59
- Tetzlaff, N., Neuhäuser, R., & Hohle, M. M. 2011, *MNRAS*, 410, 190, doi: [10.1111/j.1365-2966.2010.17434.x](https://doi.org/10.1111/j.1365-2966.2010.17434.x)
- Tody, D. 1986, Society of Photo-Optical Instrumentation Engineers (SPIE) Conference Series, Vol. 627, The IRAF Data Reduction and Analysis System, ed. D. L. Crawford, 733, doi: [10.1117/12.968154](https://doi.org/10.1117/12.968154)
- van Buren, D., & Mac Low, M.-M. 1992, *ApJ*, 394, 534, doi: [10.1086/171604](https://doi.org/10.1086/171604)
- van Buren, D., Mac Low, M.-M., Wood, D. O. S., & Churchwell, E. 1990, *ApJ*, 353, 570, doi: [10.1086/168645](https://doi.org/10.1086/168645)
- van Buren, D., & McCray, R. 1988, *ApJ*, 329, L93, doi: [10.1086/185184](https://doi.org/10.1086/185184)
- van Buren, D., Noriega-Crespo, A., & Dgani, R. 1995, *AJ*, 110, 2914, doi: [10.1086/117739](https://doi.org/10.1086/117739)
- van den Bergh, S. 2004, *AJ*, 128, 1880, doi: [10.1086/423696](https://doi.org/10.1086/423696)
- van Leeuwen, F. 2007, *A&A*, 474, 653, doi: [10.1051/0004-6361:20078357](https://doi.org/10.1051/0004-6361:20078357)
- van Marle, A. J., Meliani, Z., Keppens, R., & Decin, L. 2011, *ApJL*, 734, L26, doi: [10.1088/2041-8205/734/2/L26](https://doi.org/10.1088/2041-8205/734/2/L26)
- Vijapurkar, J., & Drilling, J. S. 1993, *ApJS*, 89, 293, doi: [10.1086/191849](https://doi.org/10.1086/191849)
- Virtanen, P., Gommers, R., Oliphant, T. E., et al. 2020, *Nature Methods*, 17, 261, doi: [10.1038/s41592-019-0686-2](https://doi.org/10.1038/s41592-019-0686-2)
- Walborn, N. R. 1971, *ApJS*, 23, 257, doi: [10.1086/190239](https://doi.org/10.1086/190239)
- Wang, Z., Kaplan, D. L., Slane, P., Morrell, N., & Kaspi, V. M. 2013, *ApJ*, 769, 122, doi: [10.1088/0004-637X/769/2/122](https://doi.org/10.1088/0004-637X/769/2/122)
- Weaver, R., McCray, R., Castor, J., Shapiro, P., & Moore, R. 1977, *ApJ*, 218, 377, doi: [10.1086/155692](https://doi.org/10.1086/155692)
- Wilkin, F. P. 1996, *ApJ*, 459, L31, doi: [10.1086/309939](https://doi.org/10.1086/309939)
- . 2000, *ApJ*, 532, 400, doi: [10.1086/308576](https://doi.org/10.1086/308576)
- Wolff, S. C., Strom, S. E., Dror, D., & Venn, K. 2007, *AJ*, 133, 1092, doi: [10.1086/511002](https://doi.org/10.1086/511002)
- Zwicky, F. 1957, *PASP*, 69, 518, doi: [10.1086/127139](https://doi.org/10.1086/127139)